Mineralogy and geochemistry of trace metals and REE in volcanic massive sulfide host rocks, stream sediments, stream waters and acid mine drainage from the lousal mine area (Iberian Pyrite Belt, Portugal)

E. Ferreira da Silva, I. Bobos, J. Xavier Matos, C. Patinha, A.P. Reis, E. Cardoso Fonseca

PII: S0883-2927(08)00419-8
DOI: 10.1016/j.apgeochem.2008.12.001
Reference: AG 1946

To appear in: *Applied Geochemistry*

Received Date: 12 October 2008
Revised Date: 21 November 2008
Accepted Date: 5 December 2008

Please cite this article as: Ferreira da Silva, E., Bobos, I., Xavier Matos, J., Patinha, C., Reis, A.P., Cardoso Fonseca, E., Mineralogy and geochemistry of trace metals and REE in volcanic massive sulfide host rocks, stream sediments, stream waters and acid mine drainage from the lousal mine area (Iberian Pyrite Belt, Portugal), *Applied Geochemistry* (2008), doi: 10.1016/j.apgeochem.2008.12.001

Mineralogy and Geochemistry of Trace Metals and REE in Volcanic Massive Sulfide Host Rocks, Stream Sediments, Stream Waters and Acid Mine Drainage From the Lousal mine area (Iberian Pyrite Belt, Portugal)

E. Ferreira da Silva[1*], I. Bobos[2], J. Xavier Matos[3], C. Patinha[1], A. P. Reis[1], E. Cardoso Fonseca[1]

[1]GeoBioTec – GeoBiosciences, Technologies and Engineering Research Center. Departamento de Geociências. Universidade de Aveiro. Campus de Santiago. 3810-193 Aveiro. Portugal eafsilva@ua.pt
[2]Departamento de Geologia. Faculdade de Ciências da Universidade do Porto. Rua Campo Alegre 687 4169 - 007 Porto. Portugal
[3]Centro de Estudos Geológicos e Mineiros de Beja, Rua Frei Amador Arrais Nº 39 r/c, Apartado 104. 7801-902 Beja. Portugal

*corresponding author, e.mail: eafsilva@ua.pt

Abstract

Acid mine drainage represents a major source of water pollution in the Lousal area. The concentrations of trace metals and the rare earth elements (REE) in the host rocks, stream sediment, surface waters and acid mine drainage (AMD) associated with abandoned mine adits and tailings impoundments were determined, in order to fingerprint their sources and to understand their mobility and water-rock interaction. The results show that the Fe-SO_4-rich acid waters vary substantially in composition both spatially and seasonally. These waters include very low pH (mostly in the range 1.9-3.0), extreme SO_4 concentrations (4635 to 20070 mg L^{-1} SO_4^{2-}), high metal content (Fe, Al, Cu, Zn and Mn) and very high REE contents. The trace metal concentrations decrease downstream from the discharge points either due to precipitation of neoformed phases or to dilution. The North-American shale composite (NASC)-normalized patterns corresponding to sediment from one stream (Corona stream) show a flat tendency or are slightly enriched in light-REE (LREE). The NASC-normalized patterns corresponding to acidic mine waters show enrichment in the middle REE (MREE) with respect to the LREE and heavy REE (HREE). Moreover, the REE concentrations in acidic mine waters are 2 or 3 orders of magnitude higher than those of the surface waters. Changes of REE concentrations and variation of Eu anomalies show two spatially distinct patterns: (a) pond and spring waters with higher REE concentrations (ranging from 375 to 2870 µg L^{-1}), that records conspicuous negative Eu anomalies, and (b) seeps from tailings impoundments corresponding to lower REE concentrations than the first pattern (ranging from 350 to 1139 µg L^{-1}) with typically negative Eu anomalies. The stream water samples collected from the impacted stream during the spring show a low pH (2.8–3.1) and contain high concentrations of Fe and trace elements (up to 61 mg/L). Also, temporal variations of the REE concentrations were observed in the Corona waters. The results obtained show that the REE concentrations increase during the winter-spring transition. Stream waters draining the

Lousal mine area show high REE concentrations, reaching a maximum value of about 2846 μg L^{-1} (spring). The MREE concentrations are usually enriched with respect to both the LREE and HREE. A decrease in REE concentrations and a pH increase from 3 to 6 was observed downstream of the confluence of a tributary stream.

The geochemistry of the waters strongly influenced the mineralogy and geochemistry of efflorescent sulfates precipitated on the banks of the streams polluted by AMD. The mineralogy is dominated by hexahydrite, rozenite, szomolnokite, alunite, gypsum, halotrychite, coquimbite, copiapite and schwertmannite. The REE concentrations determined in the efflorescent sulfates suggest a selective partitioning of the HREE onto Mg-Al-oxyhydroxides.

1. Introduction

Sulfide oxidation in mines, dumps and tailings impoundments produces acid metal-rich waters that may contaminate local surface water, groundwater and stream sediments. The resulting acid mine drainage represents a major source of water pollution in areas of present and former mining activity. Thus, mining activity, and the formation of AMD can lead to high concentrations of trace metals and REE in surface waters and groundwater.

The rare earth elements comprise the series of lanthanides and actinides. The REE acronym is commonly attributed to the lanthanide series that is strongly electropositive (electronegativity less than 1.2) and mostly trivalent (3^+) under a wide range of oxygen fugacity (Protano and Riccobono, 2002). The elements Ce and Eu can have 4^+ and 2^+ valence, giving them different properties depending on the redox potential (Olias et al., 2005). The so called ‘‘lanthanide contraction’’ is another characteristic reflecting the progressive decrease of the ionic radius from La^{3+} (1.16 Å) to Lu^{3+} (0.97 Å) (Protano and Riccobono, 2002). The REE are divided into two sub-groups: one from La to Sm (with lower atomic numbers and masses), referred to as LREE, and another from Eu to Lu (higher atomic numbers and masses), referred to ‘‘HREE. Also, the ‘‘middle rare earth elements’’ (MREE) term has been applied to the group from Nd to Gd (Sholkovitz, 1995).

REE geochemistry is an important tool in the interpretation of water-rock interactions (Worrall and Pearson, 2001). Thus, the geochemistry of REE in acidic mine waters has recently received considerable attention from several authors (Johannesson et al., 1996; Johannesson and Zhou, 1999; Verplanck et al., 1999; Marchand, 2002; Borrego et al., 2005; Gammons et al., 2005a, b; Merten et al., 2005; Olias et al., 2005; Wood et al., 2006). REE geochemistry has been applied as a potential tracer in acidic waters systems, as well as to constrain processes controlling

the fate and transport of metals in stream systems where the acidity is produced by natural processes acting on inputs from mining-impacted environments. Typically, the mobility of REE is greater in acidic than in neutral or alkaline waters, making analytical quantification relatively straightforward. Otherwise, it is well known that the REE may be fixed or sorbed to fine-grained minerals during hydrothermal or weathering processes (Bau, 1999; Nesbitt, 1979; Nasraoui et al., 2000). Several mechanisms have been discussed in the literature such as: (i) fixation in newly crystalline or amorphous phases, or (ii) sorption processes. Also, the mobilization and redistribution of lanthanides may be intensified by rapid dissolution of certain primary REE minerals through reactions with complexing ions that occur in soils and surface waters (Minarik et al., 1998). Several studies have shown a link between the dissolved REE distribution in stream sediment and the REE patterns of the dissolved minerals from altered bedrocks or load occur (Sholkovitz et al., 1999). This was explained by variable complex stabilities and preferential removal of REE from solution by colloids and newly formed minerals (Gruau et al., 2004).

The REE have largely been considered of minor environmental concern. However, some toxicological studies (Haley, 1991; Hirano and Suzuki, 1996), following the recent use of hi-tech materials in the semiconductor industry, have suggested that REE have significant pathogenic potential (Protano and Riccobono, 2002).

This research work focuses on the mobility of trace metals and REE in surface waters, stream sediment and acid waters collected in the Lousal mining area. The main goal of this work is to understand the major processes controlling trace metal and REE distribution and their interaction between stream waters, sediments and acidic waters. Thus, the role of source-rock composition, redox changes and colloidal particles on the distribution of trace metals and REE in acid mine waters, stream sediments and waters are assessed.

2. Geology and environmental setting of the study area

2.1 Geology of the area

The polymetallic massive sulfide mine of Lousal is situated in the NW region of the Iberian Pyrite Belt (IPB) (Fig. 1a) along an alignment of the Volcano-Sedimentary Complex (VSC) within the Volcanic Hosted Massive Sulfides (VHMS) province (Oliveira et al., 2001). The VSC comprises felsic volcanic and volcanoclastic rocks, black shales and detrital sediments. The Lousal mining area is limited to the north by the Espinhaço de Cão stream and to the south by the Corona stream, both tributaries to the Sado River (Fig. 1b).

The Lousal area is located in the SW limb of an anticline controlled by late stage faults with an azimuth N-S and NE-SW. The presence of stockwork structures at Lousal is associated with a metallogenetic system (Barriga and Carvalho, 1983; Barriga et al., 1997) corresponding to the brine pool model defined by Tornos et al. (2000) for Tharsis. The mineralization hosted by the VSC is related to an exhalative deposit probably formed in brine pools within the lower VSC (Upper Devonian – Lower Carboniferous). The ore deposit is characterized by the conformable upper contacts, the fine grained massive sulfides (usually pyrite-rich) and extensive hydrothermal alteration in the footwall rocks. The mineralization is dominated by pyrite, with variable amounts of chalcopyrite, galena, sphalerite, pyrrhotite, marcasite, bournonite, tetrahedrite, arsenopyrite, cobaltite, magnetite and native gold (Strauss, 1970).

2.2. Environmental setting

The Lousal mine was surface and underground exploited primarily for pyrite between 1900 and 1988. The mining legacy has resulted in a large volume of wastes (estimated to be greater than 1 Mt), ranging from barren overburden and barren rocks to various types of waste and tailings impoundments. In the Lousal mining site two tailings impoundments could be identified, one related to the mine shafts and ore mill plant (surface area of about 23907 m^2), the other close to the railway station were the mine ore was deposited and then transported (surface area of about 59542 m^2). The first area (T_B) is located in the north sector of the open pit mine, the second (T_A) is located 600m north-eastward, near the railway Lisbon-Algarve. The tailings impoundments have high concentrations of Cu, Pb, Zn, As, Cd, Sb, S and Fe, indicating that the abundant oxidized sulphidic material deposited at the time occurs in both sites (Fig.1c).

The materials are weakly cemented and locally exposed to weathering, promoting the production of AMD. Fieldwork carried out in the Lousal mine area revealed that no effective environmental measures were undertaken to constrain tailings erosion and to avoid the generation of AMD. For instance, the material used to fill the abandoned adits (basic volcanic and black shale rocks) was extracted from a quarry.

Waters from the flooded adits and wells (due to fluctuations of the water table) accumulated in the flooded quarry that became transformed into open-pit lakes. Figure 1c shows a dam (2-3 m high) constructed to retain acid waters draining from the mine and to prevent their entrance into the Corona stream. Nevertheless, the dam has intermittent leakage at its base resulting in acid water drainage into the main stream. Near the railway terminal, a big deposit of fine-grained pyrite remains intact as a small

hill. This material was never sent for treatment after the closure of the mine and is presently covered by soil (Ferreira da Silva et al., 2006).

3. Materials and Methods

3.1. Sampling and sampling preparation

The fieldwork included the identification and sampling of the different acid mine effluents and stream waters, as well as stream sediments and efflorescent salts occurring in the AMD impacted areas. In addition, samples from the massive sulfide host rocks and tailings material were collected. Sampling was performed during 3 seasonal periods: after a rainy period (winter season), during normal flow conditions (infiltration period with enrichment by dissolution – spring season), and a dry period (no precipitation – summer season).

3.1.1. Rock and pyrite ore samples

Black shales (BS), black shales with pyrite (BSPy), spilitic (SP), kaolin rocks (K) and pyrite ore (MPy) samples were collected from the study area. About 1kg of each rock sample was crushed with a jaw crusher and pulverized in a mechanical agate mill. The samples were reduced to 250g by coning and quartering, followed by drying at 40ºC. After homogenization aliquots of 30-50g of each dried sample were powdered in a mechanical agate mill.

3.1.2. Stream sediment samples:

Eight samples of sediment were collected along the Corona stream in the study area (Fig. 1b). Samples SS3 and SS4 are representative of local geochemical background, whereas samples SS6, SS8, SS9 and SS12 are representative of the AMD impacted area. Sample SS10 corresponds to Lousal stream and SS14 to Sado river. Samples were collected with a plastic spade, transferred to pre-cleaned plastic bags, sealed and brought to the laboratory. After collection, the samples were oven dried before dry sieving at a temperature of 40^{o}C, until a constant weight was attained. Samples were disaggregated and sieved through a 177µm aperture plastic sieve.

3.1.3. Stream waters and Acid Mine Drainage

The dispersion of trace metals and REE in the flowing water downstream near the Lousal mining area was determined on a suite of 8 samples distributed along a 5km tract of the Corona stream (samples SW3, SW4, SW6, SW8, SW9 and SW12) and the Sado river (SW14). Also, a reference water sample (SW10) was collected from an uncontaminated site upstream of Lousal stream (Fig. 1b).

Acid mine waters were collected from the open-pit lakes that collect water from the flooded adits (sample AMW1 – Fig. 1b), springs discharging into the impoundments (sample AMW2 – Fig. 1b) and flowing channels (water flowing from the waste piles T_A and T_B: - samples AMW18 and AMW19 Fig. 1b). Some of these sampling points are ephemeral, being active only after rainfall.

Water samples for chemical analysis were collected with syringes and Millipore standard sampling equipment. All samples were filtered in the field with 0.45 μm Millipore cellulose membrane filters and stored in clean 250mL polyethylene bottles (ASTM, 1984). Two sets of samples were collected at each site: (1) acidified to pH<2 with HNO_3; (2) unacidified for anion analysis. All of them were kept at 4 ºC prior to laboratory analyses.

3.1.4. Efflorescent sulfates

Samples containing sulfate minerals were collected near the following stations AMW2 (sample PR1), SW6 (samples PR2 and PR3), SW8 (samples PR4 and PR5), AMW18 (sample PR6), SW9 (samples PR7 and PR8) (Fig. 1b). Efflorescent salts were collected at the edge of the stream. Usually, samples with lighter colours from white, yellow, green, blue, pale-brown, ochre to red were collected and stored in polypropylene bags. The samples were kept in hermetic containers with a low air volume, far from sunlight and high temperatures, and then stored at room temperature in the laboratory. For analysis they were gently ground and mixed. Sample PR9 was obtained by high-speed ultracentrifugation and represents the colloidal particles (0.2 μm) of unfiltered acidic mine waters collected near to the AMW2 station. The samples obtained were kept at pH 3 and analyzed by X-ray diffraction and ATR-Infrared spectroscopy (Bobos et al., 2006).

3.2. Methods

3.2.1. Field parameters

Temperature (T), pH, and electric conductivity (EC) were measured in situ at each sampling location for stream water. The pH was measured with a HI 8424 microcomputer pH meter, previously calibrated against supplied calibration standards (Titrisol standard solutions) at pH 4 and pH 7 with an accuracy of measurement of about ± 0.05. Specific conductance referenced at 25ºC was measured using a HI8633 microcomputer electric conductivity meter.

3.2.1. Chemical Analyses

The powdered rock and the grain fraction (<177 μm) samples were submitted for chemical analysis and multielemental analysis to ACME (Anal. ISO 9002 Accredited Lab-Canada). The selected samples were prepared by fusion with lithium metaborate ($LiBO_2$) followed by dissolution in a multi-acid digestion (HCl-HF-HNO_3-$HClO_4$). The solutions were analyzed by ICP-MS for REE.

For trace metal analysis a 0.5g split was leached in hot (95ºC) aqua regia (HCl-HNO_3-H_2O) for 1 h. After dilution to 10 mL with water, the solutions were analyzed for 35 chemical elements by inductively coupled plasma- emission spectrometry (ICP-ES). Among these, Ag, Al, As, Bi, Cd, Co, Cu, Fe, Hg, Mo, Ni, Pb, Sb, and Zn were included in the analytical package. The detection limits for trace elements in solids were 0.3 mg kg^{-1} for As; 0.5 mg kg^{-1} for Cd; 1 mg kg^{-1} for Co, Cu, Hg, Mo, Ni and Zn; 3 mg kg^{-1} for Bi, Pb and Sb, and 0.01% for Fe.

The accuracy and analytical precision of the analytical method were verified against standard reference materials (standard SO17/CSB for major elements and REE, DS4 and DS5 standards for trace metals) and duplicate samples in each analytical set. The results were within the 95% confidence limits of the recommended values for these certified materials. Overall analytical precision was ±3% for the heavy metals and REE analyzed.

Pre-concentration of surface water samples prior to analysis was not needed, but samples with lower pH and higher total dissolved solids required dilution. The analyzed elements include major anions (Cl, NO_3 and SO_4), major cations (Ca, K, Na and Mg), REE and a suite of dissolved trace metals (Ag, Al, As, Bi, Cd, Co, Cu, Fe, Hg, Mo, Ni, Pb, Sb and Zn).

Unacidified samples were analyzed using a Dionex 1000i ion chromatography (IC) Workstation to determine the Cl, NO_3 and SO_4 concentrations. An isocratic elution with a $NaHCO_3$–Na_2CO_3 solution was employed together with a Dionex AS4-SC column. Although standards were prepared containing only the above anions, other anions would have been detected if present at levels greater than approximately 0.1 mg L^{-1}. Dilution was required for reliable anion analysis of concentrated samples. The HCO_3^- concentration was determined in situ by volumetric titration of filtered unacidified samples with H_2SO_4.

The concentrations of major cations, trace elements and REE in acidified waters were determined using an inductively coupled plasma-atomic emission spectrometry method (ICP-MS) at ACME Anal. ISO 9002 Accredited Lab - Canada. Rigorous water data quality control was performed by inserting reagent blanks and duplicate samples into each batch (Ramsey et al., 1987). The geostandard WASTWATR3 was used by ACME to check the validity and reproducibility of the results. Typical uncertainties

including error sources are <6% for all the trace elements, whereas for major anions, the uncertainties lie between 2% and 7%, depending on the concentration levels. The detection limits for major and trace elements in water samples were: 0.02 μg L^{-1} Co; 0.05 μg L^{-1} Ag, Bi, Cd, Sb; 0.1 μg L^{-1} Cu, Hg, Mo, Pb; 1 μg L^{-1} Al; 0.2 μg L^{-1} Ni; 0.5 μg L^{-1} As, Zn; 10 μg L^{-1} Fe. Values for the detection limit of the REE determinations in water samples are lower than 0.01 μg L^{-1} except for Sm (0.05 μg L^{-1}). Normalization of REE concentrations was carried out using the North American Shale Composite (NASC) according to Gromet et al. (1984).

3.3 Mineralogy

Petrography of the rock samples collected from the gossan of massive sulfide rocks was performed by optical microscopy. The <177 μm fraction of the stream sediments and the efflorescent sulfate samples were mineralogically characterized by powder X-ray diffraction (XRD) using a Philips X'Pert MPD, equipped with an automatic divergence slit, CuKα radiation (20 mA and 40 kV) and a Ni filter. Routine XRD patterns were recorded (for samples of stream sediments and efflorescent salts) from 4 to 70°2θ with a step size of 0.02°2θ with 0.5 s count time per step. The morphology of efflorescent salts were carried out by scanning electron microscopy (SEM) using a JEOL JSM-6000 instrument equipped with a Si(Li) energy-dispersive spectrometer (EDS) operating at an acceleration voltage of 20 kV, electron beam current of 1 nA and spot size of 20 nm. The samples were dried at 40ºC for 24 h and Au coated.

4. Results

4.1. Volcanic massive sulfide host rocks

Samples collected from black shales with pyrite (BSPy), black shales (BS), spilitic (SP) and kaolin rocks (K) were chemically and mineralogically analyzed. The black shales are fine grained, soft and contain abundant opaque material. The mineralogy consists of quartz-sericite matrix, rare biotite, graphitized organic matter (up to 2% of organic C) and dispersed pyrite (up to 5% of FeS_2). Titanite, zircon, rutile and apatite occur throughout the black shale as accessory minerals.

Microporphyritic basic volcanic rocks are affected by a strong spilitization process characterized by albitization of plagioclase. Spilitic rocks are constituted of chlorite, carbonates, epidote, albite, actinolite and hornblende. Also, apatite, ilmenite, titanite and zircon were observed as accessory minerals. Iron-Mn oxide/oxhyhydroxide phases cover the black shales and spilitic rocks as coatings.

Trace elements contents of black shales, spilitic and kaolin rocks are shown in Table 1. Black shales and spilitic rocks show low concentrations of trace metals,

whereas high concentrations of As and Cu were determined in kaolin rocks. The sum of the total REE (ΣREE), LREE and HREE concentrations, and the normalized $(La/Gd)_N$ and $(La/Yb)_N$ ratios of the analyzed samples are shown in Table 1. Higher concentrations of REE were found in kaolin rocks than in spilitic and black shale rocks. All samples show higher concentrations of LREE than HREE, the $(La/Yb)_N$ ranging from 0.70 to 0.97, whereas the LREE are dominant over the MREE only in the black shales. Figure 5 shows a positive Eu anomaly in spilitic rock slightly higher than the Eu anomaly in black shales and kaolin. However, kaolinite adsorbed more REE than feldspar and organic matter (Fig 5). The comparison between the results obtained in this study for spilitic basalts and those values obtained by other authors (Grimes et al., 1998) for representative samples of volcanic rocks from 5 west-trending sub-belts of the Portuguese Pyrite Belt show that the ΣREE, LREE and HREE are similar.

4.2. Waste piles and tailings impoundments

The T_A and T_B areas have different mine waste compositions (Matos and Martins 2006). The T_A area is predominantly composed of brittle pyrite ore (>60%) mixed with host rocks represented by quartz, dark grey to black shale, grey chert and felsic well cleaved quartz and rare feldspar porphyrytic volcanic. The T_B group is predominantly composed of host rocks and minor massive and semi-massive pyrite ore (<40%). Both T_A and T_B materials contain kaolinite, Fe-oxide/oxyhydroxide, sulfates and sulfides (chalcopyrite, galena, sphalerite and marcasite). The waste material of the T_B area is more coarse (centimetre to decimetre) when compared with the T_A waste material (millimetre to centimetre). Samples collected from tailings impoundments show high contents of Cu (1-1986 mg kg^{-1}), Pb (41-5981mg kg^{-1}), Zn (17-1756 mg kg^{-1}), As (6-1988 mg kg^{-1}), Cd (0.2-5.7 mg kg^{-1}), Fe (1.74-27.7%) and Al (.0.65-8.22%) (Ferreira da Silva et al., 2006).

As the presence of black shales with disseminated pyrite (BSPy) and crushed pyrite (MPy) is dominant in T_A and T_B tailings, a geochemical characterization of BSPy and MPy was performed (Table 1). Pyrite is the main sulfide phase and variable chalcopyrite, galena, sphalerite, pirrotite, marcasite, bournonite, tetrahedrite, cobaltite and native Au occur. Chemical analysis of MPy shows the following concentrations: Cu 7629 mg kg^{-1}; Pb 14009 mg kg^{-1}; Zn 237 mg kg^{-1}; As 12576 mg kg^{-1}; Sb 760 mg kg^{-1}; Ag 43.2 mg kg^{-1}; Co 159 mg kg^{-1}.

The ΣREE, LREE and HREE concentrations, and the normalized $(La/Gd)_N$ and (La/Yb)N ratios of the analyzed samples are shown in Table 1. The HREE concentrations are below the detection limit in Py, whereas the BSPy show a lower

ΣREE than the BS due to the dilution effect or to pyrite oxidation. The BSPy samples show the same pattern as the BS samples, with LREE to MREE and $(La/Gd)_N$ ratio >1.

4.3. Stream Sediment

The distribution of trace metals in stream sediment (Table 2) shows a heterogeneous pattern. Of the 3 streams sampled, the highest values of metal contamination were recorded in sediments from the Corona stream. The trace metals determined in AMD impacted stream sediment (SS6, SS8, SS9, SS12) show a large range of concentrations (278-670 mg kg^{-1} As, 0.5-5.6 mg kg^{-1} Cd, 346-1588 mg kg^{-1} Cu, 285-8523 mg kg^{-1} Pb, 385-2756 mg kg^{-1} Zn – Table 2) relative to background values measured upstream from the mines (SS3 and SS4 – Table 2) and along adjacent streams unaffected by mining activities (SS10 from the Lousal stream – Table 2). However, stream sediment sample (SS14) collected below the confluence of Lousal stream with the Sado River (Fig. 1b) shows low concentrations of trace metals, except for Cd, Cu and Zn. The high concentrations of Cd, Cu and Zn found in Sado River are similar to those values obtained in bed-load stream sediments in the Corona stream impacted with AMD. The tendency of Cd, Cu and Zn to accumulate in sediments could be related to the presence of kaolinite and sulfates identified by XRD. The highest concentrations of Fe (10.5-19.0%) and Al (8.9-14.5%) also occur in the sediments located around the open-pit lakes, mine wastes and tailings impoundments (T_A and T_B – Fig. 1c) as explained by the large amounts of Fe oxy-hydroxide and sulfates precipitated during drying periods.

The <177μm grain fractions collected from the Corona stream are dominated by quartz and lesser amounts of feldspars, clays and Fe-Mn oxide/oxhyhydroxide. The fine fractions separated from the sediments consist of kaolinite, mica, chlorite and Fe-oxyhydroxides (Cardoso Fonseca and Ferreira da Silva, 2000).

The concentrations of REE and the normalized concentration ratios of La/Yb_N and La/Gd_N for stream sediment samples are shown in Table 2. The ΣREE range from 96.9 to 189.9 mg kg^{-1} and no significant variations of the LREE/HREE ratio (6.00 to 8.03) characterize the bed-load stream sediment samples. Cerium is the most abundant element of the LREE in all the analyzed stream sediment samples. No significant variation is observed along the Corona stream for the LREE/HREE ratio. Most of the samples show a La/Yb_N >1 meaning an enrichment in LREE in the Corona stream sediment. The ratio of La/Gd_N <1 suggests a moderate enrichment in MREE relative to LREE.

4.4. Acid mine waters

The most important AMD discharges come from the open-pit lakes that collect water from the flooded adits (AMW1), spring discharging into the impoundments (AMW2) and flowing channels (AMW18 and AMW19). Field parameters and chemical composition of the studied acid mine waters samples are reported in Table 3. The pH values measured on acidic waters emerging from the tailings range from 1.9 to 3.0, and a high conductivity (up to 24 mS cm^{-1}) and high concentration of dissolved SO_4^{2-} (up to 20070 mg L^{-1}) were found. These waters are also significantly enriched in Al, Fe and trace metals (Fig. 2a to 2f). According to the relative concentration of major and minor ions, using the conventional Piper diagram (Freeze and Cherry, 1979), these waters in terms of the major anion facies are classified as SO_4^{2-}-type while the cation facies is Fe-Mg(Ca) type. Both water volume and chemical composition of the acidic waters vary seasonally. These waters plot in the field of "high acid/extreme metal (A)" in the Ficklin diagram (Fig. 3a)

The ΣREE, LREE and HREE concentrations and the normalized concentration ratios of $(La/Yb)_N$ and $(La/Gd)_N$ in the acidic mine water samples are shown in Table 4. Selected samples exhibit a broad range of ΣREE concentrations from 372 μg L^{-1} (sample AMW1) to 2846 μg L^{-1} in sample AMW2. The data obtained show that the chemistry is similar to that of other acidic waters described elsewhere (Johannesson and Lyons, 1995; Gimeno Serrano et al., 2000; Protano and Riccobono, 2002; López González et al., 2005). The results show also that the REE concentrations increase during the spring and summer periods. Enrichment of LREE relative to HREE is observed in samples AMW1 and AMW2, with the ratio $(La/Yb)_N$ >1 in all seasons, while the ratio $(La/Yb)_N$ <1 for samples AMW18 and AMW19 means an enrichment of HREE relative to LREE (Table 4). Also, the samples show similar $(La/Gd)_N$ ratio so that all these waters are MREE enriched.

4.5. Surface Stream Waters

The physical parameters and concentrations of trace metals and REE determined in the surface stream waters are reported in Table 5a, 5b and 5c. The Corona stream waters flowing from upstream of the Lousal mine site (SW3 and SW4) correspond to a HCO_3-Ca type composition. The chemical composition of the SW3 and SW4 waters show lower SO_4^{2-} and Cl^- concentrations with respect to HCO_3^- content (alkalinity equivalent to 200 to 400 mg L^{-1} HCO_3^-) and no clear chemical distinction between these waters and those from the Lousal stream (SW10) is observed. The hydrogeochemical facies of these waters become progressively SO_4-Fe(Ca) type (Ferreira da Silva et al., 2006) towards the mining area (samples: SW6 to SW9). In all cases the unaffected surface waters are characterized by circumneutral pH, low conductivity values and

relatively low metal concentrations during all seasons. The waters affected by AMD are highly mineralized (electrical conductivity of up to 2180 µS/cm), and show neutral to low pH values (7.3 to 3.2) depending on the season and the distance from the AMD sources (Figs 2 and 3c). According to Ferreira da Silva et al., (2005), the waters reveal an increase in trace metal concentrations relative to the background concentrations (Cu exceeds its background level by 11-1179 times, Pb about 58-248 times, Zn 70-424 times) and As (5-611 times). Moreover, high concentrations of Fe (7380 – 61600 µg L^{-1}), Al (3460 – 35409 µg L^{-1}), and SO_4^{2-} (528-1306 mg L^{-1}) were measured which is consistent with those values expected in mining impacted areas with waste deposits and tailings impoundments (Reimann and de Caritat, 1998).

As acidic stream waters flow downstream (SW9 to SW12) they become progressively neutralized due to dilution effects of Lousal water that flows into the stream. The pH increases and dissolved ions begin to precipitate as neutralization occur (Fig. 2).

The ΣREE and the normalized concentration ratios of $(La/Yb)_N$ and $(La/Gd)_N$ of the stream waters samples are shown in Table 5a, b and c. The concentrations of REE in the representative samples related to the geochemical background (SW3, SW4 and SW10) are lower (winter: 0.14-1.04 µg L^{-1}; spring: b.d.l.-1.66 µg L^{-1}; summer: 0.98-7.62 µg L^{-1}) than those samples collected in the impacted area of Corona stream (SW6, SW8, SW9, SW12) (winter: 2.79-4.09 µg L^{-1}; spring: 38.7-69.9 µg L^{-1}; summer: 79.7-381.7 µg L^{-1}). Also the ΣLREE/ΣHREE corresponding to geochemical background samples show higher values than those found in samples collected in the impacted Corona stream (Table 5a, 5b and 5c).

Samples collected in the impacted area of the Corona stream show a $(La/Gd)_N$ <1 ranging from 0.10 to 0.59 (Table 5a, 5b and 5c), while the representative samples corresponding to the geochemical background show values of $(La/Gd)_N$ >1 (with the exception of SS3 collected during the spring and summer periods). The $(La/Yb)_N$ ratio also ranges from 0.87 to 2.64 showing that the samples from the impacted area of Corona stream, are mostly enriched in LREE relative to HREE (except sample SW12 collected during the summer period - $(La/Yb)_N$ = 0.31).

4.6. *Efflorescent sulfates*

A great variety of sulfates occurring around the open-pit lake in the Lousal area were identified by XRD. Attention was focused on the poorly- and well-crystallized sulfate sequence beginning with the simple hydrated salts from divalent to trivalent cations. They are characterized as monomineralic or combined phases and consist of: EF1: hexahydrite [$MgSO_4.6H_2O$]; EF2: rozenite [$Fe(SO_4).4H_2O$], EF3: szomolnokite

[$Fe(SO_4).H_2O$]; EF4: rozenite, alunite [$KAl_3(SO_4)_2(OH)_6$], gypsum [$CaSO_4.2H_2O$] and halotrichite [$FeAl_2(SO_4)_4.22H_2O$]; EF5: alunite, rozenite and gypsum; EF6: copiapite [$(Fe,Mg)Fe_4(SO_4)_6(OH)_2.20H_2O$] and coquimbite [$Fe_2(SO_4)_3.9H_2O$]; EF7 and EF8: gypsum, rozenite, alunite and kaolinite; EF9: schwertmannite [$Fe_8O_8(SO_4)\ (OH)_6$]. Most of these phases have been identified in other AMD related studies (Alpers et al., 1994; Nordstrom, 1982; Nordstrom and Alpers, 1999; Buckby et al., 2003; Romero et al., 2006b). In the present case, hexahydrite, rozenite, szomolnokite and halotrichite are the dominant phases at the discharge points of the more acidic waters (AMW2 and AMW18), whereas coquimbite and copiapite are typical of the banks of the stream affected by AMD (SW9).

Scanning electron microscopy shows that natrojarosite crystals are pseudo-cube-like rhomb, ranging from 1 to 1.5 μm in diameter (Fig. 4a). Coquimbite crystals show an acicular habit with random aggregates or needles of fine aciculae, where the length of aciculae ranges from 6 to 18 μm (Fig. 4b). Also, needles of halotrichite - pickeringite are observed in the same figure. Copiapite exhibits a pseudo-hexagonal platy morphology (Fig. 4c), but sometimes were identified as thin plates which formed rosette-shaped intergrowths. Larger platy-crystals of copiapite were associated with the Mg-copiapite. Alunite shows a cube-like rhombic morphology, whereas gypsum exhibits a flower-like morphology (Fig. 4d). Two distinct shapes of copiapite were observed: platy (Mg-copiapite) and fibrous needles (Al-copiapite) (Fig. 4e). Aggregates of halotrichite - pickeringite displaying a lath-like habit or needles are shown in Figure 4f.

The trace metal and REE concentrations of mineral assemblages are shown in Table 6. Chemical analysis reveals a higher concentration of Cu (1966 mg kg^{-1}- Table 6) in hexahydrite, whereas high concentrations of Zn were recorded in rozenite (EF2) and in the assemblage of alunite, rozenite and gypsum (EF4, EF5, EF7, EF8 – Table 6). Moreover, highest concentrations of As and Cu were recorded in the samples EF5 and EF6 corresponding to the copiapite, coquimbite, or gypsum, alunite, rozenite assemblage. Sample EF5 shows high concentrations of Zn (11250 mg kg^{-1}). Lower concentrations of trace metals compared with other samples analyzed were found for szomolnokite (EF3). Lower concentrations of bivalent trace metals and high concentrations of As and Pb were recorded in samples of schwertmanite (EF9). According to Gosselin et al. (1992), acidic waters prevent Cu, Mn and Zn from adsorbing strongly onto the schwertmanite surface. In contrast, As partitioned strongly into the precipitates and could be due to the anionic form of dissolved As in oxidized waters ($H_2AsO_4^-$) which – like sulfate – should adsorb strongly onto the positively charged surfaces of freshly precipitated scwertmannite at pH<3 .

Two distinct efflorescent sulfate groups could be differentiated based on the REE abundances (Table 6). The first sample group (EF3, EF7, EF8 and EF9) displays a very high REE concentration (ΣREE = 85.2 to 124.2), whereas the second sample group (EF1, EF4, EF5 and EF6) displays a lower REE concentration (ΣREEs = 7.93 to 45.1). Compared to the second group, the first group is characterized by higher ΣLREEs (ranging from 76.9 to 105.9), ΣLREEs/ΣHREEs (ranging from 5.75 to 9.32), and ratios of $(La/Yb)_N$ higher than one (1.91 to 2.08). All samples have ratios of $(La/Gd)_N < 1$ (Table 6), and chemical data indicate the presence of Ce (2.6-48.7 mg kg^{-1}), La (1.2-21.7 mg kg^{-1}) and Nd (up to 27.7 mg kg^{-1}).

5. Discussion

When normalized against NASC, the REE patterns of the VMS host rocks (Fig. 5) show a flat to slightly increasing MREE trend. The patterns also reveal a small to moderately positive Eu anomaly, where the values range from 1.40 (kaolin rocks) to 1.60 (spilitic rocks). Both samples analyzed had been affected by kaolinization and albitization of volcanic rocks during hydrothermal venting. REE patterns for the sulfide-bearing shales (BSPy) show a Ce depletion and a positive Eu anomaly. A negative Ce anomaly could be related to oxidation of organic matter or due to the extensive weathering removal of the other REE (Aström and Corin, 2003; Worrall and Pearson, 2001). This could explain the lower REE concentrations in BSPy relative to BS.

The data show that the kaolin samples have LREE enrichment and a slight positive Eu anomaly. The LREE enrichment reflects the results of extreme weathering while the slight positive Eu anomaly is due to partially altered plagioclase presence in the kaolin rocks (Nyakairu et al., 2001). The REE are released from primary minerals (i.e., feldspars) and taken up by the secondary phases during kaolinization (Nesbitt, 1979). REE adsorption onto kaolin surfaces shows clear pH dependence. Dominant electrostatic interaction and specific site binding due to the negatively charged kaolinite surface occur at low pH from 3 to 4 (needed for kaolin formation) which enhanced the REE adsorption (Wan and Liu, 2006; Coppin et al., 2002). A Ce anomaly is lacking (0.95-1.03) in these host rocks due to there being no Ce oxidation conditions.

During the rainfall periods the infiltrated water interacts with the mineral phases in the tailings. The oxidation reactions involved sulfide minerals (pyrite and marcasite) and induced quite low pH values in these waters, which in turn favour the dissolution of particularly sensitive phases.

AMD represents a major source of water pollution in the Lousal area, and is characterized by low pH and high total dissolved metals. Chemical composition of the studied waters show high contents of SO_4^{2-} and metal concentrations such as Zn, Cu

(and to a lesser degree Pb, Cd, Co and Ni, together with As) which is a common feature of mine waters draining massive sulfide deposits (Ball and Nordstrom, 1991; Plumlee et al., 1999; Nordstrom and Alpers, 1999; Sánchez Espanã et al., 2005). The concentrations of Zn, Cu, Pb, Cd, As, Co, Ni and Mn increase as SO_4^{2-} content increases due to progressive oxidation of pyrite and other sulfide minerals (Fig. 2c). Water compositions show a chemical variation from the winter to summer seasons (Tables 5a to c). These variations could be explained by the combination of several factors, other than dilution by freshwater after rainfall episodes, such as: the dissolution of efflorescent sulfates previously formed during the dry period and the mineralogical differences between the mineralization being oxidized and the host rocks.

The acid mine waters AMW1 and AMW2 show (Table 3) lower concentrations of Al (22 – 136 mgL^{-1}), Fe (14.5 – 959 mg L^{-1}) and As (b.d.l -95 µg L^{-1}) when compared with samples AMW18 and AMW19 (Al: 327 – 1100 mg L^{-1}; Fe: 1526 – 8215 mgL^{-1}; As: 4574 – 36455 µg L^{-1}).

The REE concentrations increase as the pH of acid mine waters decreases. (Tables 3, 5a, b, c). The REE abundances determined exceed those of normal fresh waters (neutral pH) by 2 - 3 orders of magnitude. Two types of REE patterns were observed in acid mine waters (Fig. 6). Samples AMW1 and AMW2 display a MREE enriched pattern with a negative Eu anomaly, while samples AMW18 and AMW19 display a MREE enriched pattern with a positive Eu anomaly. Therefore, the negative Eu anomaly (0.55 to 0.75) observed in samples AMW1 and AMW2 (waters that react significantly with rocks along the flooded deep galleries) are inherited from the felsic volcanic rocks. The positive Eu anomalies (1.46 to 1.95) could be inherited from the host rocks where the waters acquired their REE concentration (see Fig. 5 – BSPy and SP are characterized by a flat REE pattern with a positive Eu anomaly). It is likely that most of the Eu is contained in plagioclase. Otherwise, the negative Eu anomaly of acidic mine waters *(*i.e., AMW1 and AMW2) may be more reduced than the other waters because they are related to deep flooded adits. Europium in the divalent state would be more readily leached from the BSPy, SP or kaolin rocks than the trivalent REE.

The presence or absence of Ce anomalies in acid waters was also observed (Table 4). The negative Ce anomaly (values range from 0.68 to 0.89) is relatively common in oxidized waters, suggesting Ce(III) oxidation to Ce(IV) under the prevailing oxidizing conditions of acid waters. The negative anomaly was identified mainly in samples collected during the spring and summer season, being also associated with the sorption/precipitation reactions (Miekeley et al., 1992). Cerium anomalies have also been observed in shallow groundwater samples, after the oxidation of Ce(III) to

558 insoluble Ce(IV), with subsequent removal from solution (Smedley, 1991). The loss of
559 Ce relative to its neighboring REE (La and Pr) produces a negative Ce anomaly in the
560 REE patterns. Positive Ce anomalies are associated with local anoxia (Table 4).

561 The NASC-normalized REE patterns of the acid mine waters are dominated by a
562 distinct convexity centered on Eu/Gd that reflect an enrichment of MREE over both
563 LREE and HREE. Thus, similar patterns have been previously reported in acidic waters
564 where SO_4^{2-} is the dominant anion (Johannesson and Lyons, 1995; Nordstrom et al.,
565 1995; Elbaz-Poulichet and Dupuy, 1999; Gimeno Serrano, 1999; Johannesson and
566 Zhou, 1999; Gimeno Serrano et al., 2000; Worral and Pearson, 2001).

567 The MREE in acid waters are preferentially enriched over the LREE and HREE,
568 due to acid leaching of Fe-Mn-oxides/oxyhydroxides (Gosselin et al., 1992;
569 Johannesson and Zhou 1999). Acid mine waters involve a large variety of inorganic
570 complexes with a great ability to develop complexation reactions that could play an
571 important role in REE fractionation. In this study the most important inorganic ligand
572 present in abundance in the acid mine waters is SO_4^{2-} (4850 mg L^{-1} to 20070 mg L^{-1}).
573 According to several authors the free metal ions Ln^{3+} (Ln refers to any lanthanide
574 element) may complex with SO_4^{2-} forming more stable $LnSO_4^{+}$, which it is one of the
575 dominant forms of dissolved REE (Johanneson and Lyons, 1995; Tabaksblat, 2002;
576 Zhao et al., 2007).

577 Also, it is well known that the concentrations of SO_4^{2-}, Al, Fe, Mn, trace metals
578 and REE in acid mine waters show strong seasonal influence (Alpers et al, 1994;
579 Kimball, 1999; Kimball et al., 2007; Nagorski et al., 2003a,b). The oxidation of tailings
580 material is responsible for the AMD production, whereas in the dry period the major
581 AMD input comes from the leaky dam. As shown in Figure 6 the acidic mine water
582 samples in the different sampling periods show minor variations in REE distribution
583 patterns, despite the varying REE concentration from winter to summer. Thus, the REE
584 patterns are independent of REE concentration.

585 Precipitation of Al- and Fe- oxyhydroxide and Fe-oxyhydroxysulfates during the
586 summer period plays an important role in the fixation of trace metals, regulating
587 dissolved trace metal concentrations through adsorption. The adsorption of trace
588 metals is affected by the presence of SO_4^{2-} which is sorbed in outer or inner spheres of
589 schwertmannite or even on ternary surface complexes ($FeOHMeSO_4$), where
590 adsorption of trace metals increases at lower pH (Bobos et al., 2006).

591 Melanterite and szomolnokite were the first to form as a result of pyrite or
592 marcasite oxidation. The formation of melanterite is related to the first stage of pyrite
593 oxidation, when water is rich in Fe^{2+} (Blowes et al., 1991). A general paragenesis
594 sequence has resulted from the natural dehydration and decomposition products of

melanterite in the Lousal area. Rozenite (EF2, EF4, EF7 and EF8) frequently, results from melanterite dehydration, and is widely distributed in the study area. Hexahydrite (EF1) also may result from the dehydration of epsomite (Alpers et al., 1994; Jambor et al., 2000) during dry periods with temperatures ranging from 30 to 40^{0}C. The epsomite precipitated from Mg-rich AMW2 acidic water (621-1264 mg L^{-1}). The pH is near 3 and ochreous mineral precipitation removes Fe and allows Mg to become dominant (Romero et al., 2006a). The precipitation of Fe- oxyhydroxides is one of the main factors involved in the occurrence of Mg sulfates. The occurrence of coquimbite (EF6) in the acidic stream of Corona (near sample AMW18) is in agreement with the results reported by other authors (Buckby et al., 2003; Jerz and Rimstidt, 2003; Romero et al., 2006b) and implies that Al and Fe^{3+} are preferentially removed from the water and fixed in sulfates. This caused the relative enrichment in Mg, which is confirmed by the occurrence of Mg - copiapite (EF6). Mixed divalent-trivalent salts are characterized by the presence of halotrichite, copiapite and römerite. A wide range of substitutions by Al, Mg, Na, Cu and Zn may occur in copiapite resulting in new sulfates such as: coquimbite, paracoquimbite, römerite or even natrojarosite, and alunite. Gypsum also occurs in these acidic environments due to the availability of alkalis used for the pH neutralization. This agrees with some related studies from other impacted AMD areas (e.g. Karathanasis et al. 1988; Alpers et al., 1989; Bigham et al., 1990, 1996; Ritsema and Gronenberg, 1993; Balkenhol et al. 2001; Lugwig et al., 2001).

The concentrations of trace metals determined in mineral-assemblage sequences are strictly related to the crystal chemistry of hydrated sulfates. Simple hydrated sulfates with divalent metal cations show interesting characteristics in their order of metal absorption. Higher amounts of Zn were recorded in rozenite, possibly related to Zn substitutions for Fe in the structure of the minerals, or adsorbtion. By contrast, the hexahydrite sample (EF1) has a higher Cu concentration and lower concentrations of trace metals than the szomolnokite sample (EF3). Higher concentrations of As, Cu and Zn have also been observed in the samples with copiapite, coquimbite and alunite.

The NASC-normalized REE patterns for the efflorescence sulfates show two distinct groups (Fig. 7). The first group demonstrates the typical characteristics of MREE-enriched NASC-normalized REE pattern (Fig. 7a), while the second group shows a shape that indicates a strong enrichment of HREE (Fig. 7b). The first group is related with to Fe-rich efflorescent salts, while the second group is related to efflorescent phases that show a significant Mg- and Al enrichment. The precipitation of sulfates related to the first and second group occurred at a pH > 3. However, sample EF6 characterized by copiapite and coquimbite precipitated at a pH < 3. Considerable proportions of REE concentrations occur at pH > 3.

The highest Fe concentration produces minor changes in $LnSO^{+}_{4}$ complexes and thus, in the REE speciation scheme, whereas a significant Mg and Al enrichment caused a strong HREE enrichment. REE occur predominantly as sulfate complexes, but the relative proportions of Ln^{3+} and $LnSO^{+}_{4}$ are related to pH and the type of crystal-chemistry of the sulfate precipitated (Wood et al., 2006; Leybourne et al., 2000). The results suggest that these sulfates play an important role in the transient storage of metals and acidity that can be easily re-dissolved during rainfall episodes and incorporated into the waters of the Corona stream. Dominant trace metals in the impacted zone of the Corona stream waters by AMD are Cu and Zn (Tables 5a, b and c). No other trace metals occur either in the Sado or in Lousal streams.

The relative abundance of REE concentration in the Corona stream waters analyzed during spring and summer is far higher than during the winter, showing a clear influence of dilution in the winter. Also, the REE concentrations of the Lousal stream waters or from the non-contaminated Corona stream waters (SW3 and SW4 – Tables 5a, b and c) are lower than those reported for the impacted Corona stream.

As acidic waters flow downstream, they become progressively neutralized by possible dilution with clean water (SW10) flowing into the Corona stream. As neutralization occurs and pH rises, dissolved ions begin to precipitate. The removal of REE occurs close to the confluence of the Corona stream with the Sado River, represented by sample SW12 (Table 5a), due to the precipitation of these elements in the sediments which are enriched by a factor of 10^{2}-10^{4} relatively to the stream waters.

The NASC-normalized REE patterns of the impacted stream waters throughout the different seasons also show strong variations (Fig. 8a, b and c). During the winter pH values increased (ranging from 6.8 to 7.5) and the trace metals and REE concentrations decreased due to a dilution process and chemical attenuation (Table 5a). Similar results were obtained by (Goldstein and Jacobsen, 1988; Elderfield et al., 1990; Dupre et al., 1996; Bau, 1999; Landa et al., 2000). Also, the REE distribution in stream waters shows a clear convex pattern (Fig. 8a), meaning that MREE are enriched with respect to LREE and HREE. The convex-upward pattern assumed to be due to MREE enrichment was caused by acidic waters (inflow samples AMW18 and AMW19). Behind a clear enrichment of MREE, the NASC-normalized REE pattern of stream waters shows a drop in Ce concentration during spring (Fig. 8b). This probably reflects the oxidation of Ce^{3+} to Ce^{4+} and its removal from solution because of its high surface reactivity with respect to the adjacent trivalent REE (Byrne and Kim, 1993). Cerium is absorbed preferentially by Fe-oxyhydroxide at low pH values (Bau 1999). The results of Gammons et al. (2003) indicate a preferential partitioning of Ce in the ferric precipitates. Surface waters frequently show more or less pronounced negative

Ce anomalies (Elderfield et al., 1990; Smedley, 1991; Miekeley et al., 1994; Leybourne et al., 2000; Johannesson et al., 1996). The data strongly support the conclusions of Leybourne et al. (2000) concerning rapid development of these anomalies in surface waters. The decreasing trend from Eu to Lu is due to selective partitioning of HREE into suspended colloidal particles or secondary minerals.

Previous studies of REE in stream waters impacted by AMD have shown that the REE tend to partition onto suspended particles of hydrous metal oxides at a pH roughly greater than 5.5 (Verplanck et al., 2004). The pH-dependence of solid-aqueous partitioning of REE appears to be controlled by an adsorption edge of aqueous lanthanide ions onto HFO and HAO surfaces, which could occur at near pH = 5.2 and 5.5 (Bau, 1999; Coppin et al., 2002; Verplanck et al., 2004). Furthermore, the LREE are partitioned to the suspended solids to a lesser extent than the MREE and HREE (Verplanck et al., 2004; Gammons et al., 2005a). These results are consistent with those of REE patterns for sulfates shown in Figure 7a that precipitate during dry seasons when the evaporation process increases.

The enrichment of the stream sediments in As, Cu, Pb, Zn and Cd appears to be mainly due to the erosion and dismantling of the tailing deposits, which provide sulfide inputs to the main stream. However, other mechanisms contribute to the secondary dispersion of the metals, such as: a) precipitation of hydroxide, oxyhydroxide, or hydroxysulfate phases from aqueous species due to the increase of pH; and b) adsorption of metals onto surfaces of these neoformed minerals (carbonates or on Fe and Mn coatings, for example), according to Nordstrom (1982) and Smith (1999).

The REE distribution related to stream sediments collected from both the Corona and Lousal streams and the Sado River shows a fairly distinct variation (Fig. 9). The results show essentially flat normalized REE profiles, indicating that the stream sediments samples had a REE pattern similar to NASC which itself is thought to represent the average composition of the Earth's continental crust. The NASC-normalized REE patterns of stream sediment are characterized by a slight enrichment in LREE and a slight depletion in HREE (Fig. 9). The pattern is probably inherited from the source area (black-shales and felsic rocks) and is also due to the mixing and homogenizing of sediments (Sholkovitz 1995). Significant variations of Ce/Ce* (0.95-1.02 – Table 2) were not observed from the upstream to the downstream areas in the Corona stream. The Eu/Eu* values mostly vary between 0.89 and 0.98 (Table 2) indicating the virtual absence of any significant Eu anomaly.

6. Conclusions

Lower concentrations of trace metals were measured in black shales and spilitic rocks than in the mineralized black shales and kaolin rocks. Kaolin rocks display higher REE concentrations than spilitic or black shale rocks. The bed-load stream sediment shows a moderate MREE enrichment relative to LREE.

The chemical composition of acid mine waters in the Lousal mine show variations in response to climatic, hydrogeological and mineralogical factors. Erosion, dismantling and transport of the tailing impoundments added sulfide minerals into the Corona stream promoting toxic metal enrichment in stream sediments. Also, weathering, mineral dissolution during rainfall, secondary dispersion, precipitation of Fe-oxyhydroxides, sulfates and adsorption of metals onto surfaces of the neoformed minerals have contributed to the geochemical re-cycling of trace metals and REE.

The results indicate a link between the measured concentration of SO_4^{2-} and REE in both acidic mine and stream waters (Fig. 2). Thus, SO_4 is the principal ligand, where, in acid waters, the REE occur as SO_4 complexes more than free ions. Otherwise, Fe in high concentrations in the acidic waters shows negligible competition for ligands with REE (Gimeno Serrano et al., 2000). In the speciation scheme, minor changes in $LnSO_4^+$ complexes are produced in the presence of high Fe concentration, whereas a significant Mg and Al enrichment caused a strong HREE enrichment.

The waters from springs (AMW1 and AMW2) show a Eu negative anomaly, while the acidic mine waters that derive from the rain-wash of tailings (AMW18 and AMW19) impoundments show a positive Eu anomaly (Fig. 6b).

Surface waters from Corona stream have low pH values and high concentrations of SO_4, REE and other metals (Cu, Pb, Zn, Cd, As, Fe and Al) near the mining region (impacted stream). The pH values and concentrations of SO_4, Al, Fe, Cu, Ni, Pb, Zn, Mn and REE measured in stream waters show seasonal variations. The total REE concentrations of surface water samples are rather variable, reaching up to 323 mg L^{-1}. Mixing of the Corona acidic mine waters with unpolluted stream waters (e.g Lousal stream – SW10) is responsible for the decrease of the REE concentrations, where pH has played an important role in the REE fractionation. The NASC-normalized pattern of the most-contaminated points with acid mine waters show a MREE enrichment during the spring season (Fig. 8b) with respect to LREE and HREE. The Ce-anomaly becomes more negative as pH increases, due to Ce fractionation under the prevailing oxidizing conditions of acid waters and to the sorption/precipitation reactions (Miekeley et al, 1992).

The evaporation of acid mine waters caused the precipitation of efflorescent minerals which are temporary reservoirs of acidity, metals and REE. The results suggest that precipitated sulfate minerals play an important role in the transient storage

of metals and acidity that can be easily dissolved during rainfall episodes. The NASC-normalized REE patterns corresponding to the efflorescent sulfates display two distinct groups: one showing a MREE-enriched pattern associated with the Fe-rich efflorescent sulfates, while the second group displays a strong HREE enrichment characteristic of Mg- and Al- efflorescent minerals. The REE are absorbed by sulfate complexes, where the relative proportions of Ln^{3+} and $LnSO^{+}_{4}$ are related to pH and the type of crystal-chemistry of the sulfate mineral precipitated.

Acknowledgements

This study was made possible with the financial support provided by IAPMEI - Ministério da Economia. Particular acknowledgment is addressed to Instituto Geológico e Mineiro (INETI Inovação) for authorizing the use and publishing of the geochemical and hydrochemical data from the Project "*Estudo do Controle Ambiental nas áreas mineiras abandonadas de Lousal e Caveira*". We gratefully acknowledge Dr. Briant Kimball, Prof. Emílio Galán, and the anonymous reviewer whose comments and suggestions significantly improved the manuscript. The paper benefited also from the fruitful comments of Dr. Kirk Nordstrom. Many thanks are due to Dr. Deborah Martin and Sónia Rodrigues for help with the English text.

References

Alpers, C.N., Nordstrom, D.K., Ball, J.W., 1989. Solubility of jarosite solid solutions precipitated from acid mine waters, Iron Mountain, California, USA. Sciences Geologiques Bull. 42, 281–298.

Alpers, C.N., Nordstrom, D.K., Thompson, J.M., 1994. Seasonal variations of Zn/Cu ratios in acid mine water from Iron Mountain, California. In: Alpers, C.N., Blowes, D.W. (Eds), Environmental Geochemistry of Sulfide Oxidation. Am. Chem. Soc. Symp. Ser. 550, 324-344.

ASTM, 1984. American Society for Testing Materials, Annual Book of ASTM Standards. Water Environmental Technology 11.01.

Aström, M., Corin, N., 2003. Distribution of rare earth elements in anionic, cationic and particulate fractions in boreal humus-rich stream affected by acid sulphate soils. Water Res. 37, 273-280.

Balkenhol, R., Ludwig, B., Ufer, K., Jochum, J. , Friedrich, G., 2001. Pyrite oxidation in sediment samples from the German open-cut brown coal mine Zwenkau: mineral formation and dissolution of silicates. J. Plant Nutr. Soil Sci. 164, 283-288.

Ball, J.W., Nordstrom, D.K., 1991. User's manual for WATEQ4F, with revised thermodynamic data base and test cases for calculating speciation of major, trace, and redox elements in natural waters. U.S. Geol. Surv. Open-File Report 91–183.

Barriga, F.J.A.S., Carvalho, D., 1983. Carboniferous volcanogenic sulphide mineralizations in south Portugal (Iberian Pyrite Belt). Memórias dos Serviços Geológicos de Portugal 29, 99-113.

783 Barriga, F.J.A.S., Carvalho, D., Ribeiro, A., 1997. Introduction to the Iberian Pyrite Belt. In:
784 Barriga, F.J.A.S., Carvalho D. (Eds), Geology and VMS Deposits of the Iberian Pyrite Belt.
785 Society of Economic Geologists Guidebook Series, Colorado 27, 1-20.
786 Bau, M., 1999. Scavenging of dissolved yttrium and rare earths by precipitating iron hydroxide:
787 experimental evidence for Ce oxidation, Y-Ho fractionation, and lanthanide tetrad effect.
788 Geochim. Cosmochim. Acta 63, 67–77.
789 Bigham, J.M., Schwertmann, U., Carlson, L., Murad, E., 1990. A poorly crystallized
790 oxyhydroxysulfate of iron formed by bacterial oxidation of Fe(II) in acid mine waters.
791 Geochim. Cosmochim. Acta 54, 2743-2758.
792 Bigham, J.M., Schwertmann, U., Traina, S.J., Winland, R.L., Wolf, M., 1996. Schwertmannite
793 and the chemical modeling of iron in acid sulfate waters. Geochim. Cosmochim. Acta 60,
794 2111-2121.
795 Blowes, D.E., Reardon, E.J., Jambor, J.L., Cherry, J.A., 1991. The formation and potential
796 importance of cemented layers in inactive sulfide mine tailings. Geochim. Cosmochim. Acta
797 55, 965-978.
798 Bobos, I., Durães, N., Noronha, F. 2006. Mineralogy and geochemistry of mill tailings
799 impoundments from Algares (Aljustrel), Portugal: Implications for acid sulfate mine waters
800 formation. J. Geochem. Explor. 88, 1-5.
801 Borrego J., López-González N., Carro B., Lozano-Soria O., 2005. Geochemistry of rare-earth in
802 Holocene sediments of an acidic estuary: Environmental markers (Tinto River Estuary,
803 South-Western Spain). J. Geochem. Explor. 86, 119-129.
804 Buckby, T., Black, S., Coleman, M. L., Hodson, M. E., 2003. Fe-sulphate-rich evaporative
805 mineral precipitates from the Rio Tinto, southwest Spain. Mineral. Mag. 67, 263-278.
806 Byrne, R.H., Kim, K.H., 1993. Rare earth precipitation and coprecipitation behaviour. The
807 limiting role of PO_4 on dissolved rare earth concentrations in seawater. Geochim.
808 Cosmochim. Acta 82, 1839-1863.
809 Cardoso Fonseca, E., Ferreira da Silva, E., 2000. Projecto Estudo de Controle Ambiental nas
810 Áreas Mineiras Abandonadas de Lousal e Caveira. Relatório Técnico Final da
811 Universidade de Aveiro (unpublished).
812 Coppin, F., Berger, G., Bauer, A., Castet, S., Loubet, M., 2002. Sorption of lanthanides on
813 smectite and kaolinite, Chem. Geol. 182, 57-68.
814 Dupre, B., Gaillardet, J., Rousseau, D., Allegre, C.J., 1996. Major and trace elements of river-
815 borne material: the Congo basin. Geochim. Cosmochim. Acta 96, 1301-1321.
816 Elbaz-Poulichet F., Dupuy C., 1999. Behaviour of rare earth elements at the freshwater-
817 seawater interface of two acid mine rivers: the Tinto and Odiel (Andalucia, Spain). Appl.
818 Geochem. 14, 1063-1072.
819 Elderfield, J., Upstill-Goddard, R., Sholkovitz, E.R., 1990. The rare earth elements in rivers,
820 estuaries and coastal seas and their significance to the composition of ocean waters.
821 Geochim. Cosmochim. Acta 54, 971-991.

822 Ferreira da Silva, E., Matos, J., Patinha, C., Reis, P., Cardoso Fonseca, E., 2005. The effect of
823 unconfined mine tailings on the geochemistry of soils, sediments and surface waters of the
824 Lousal area (Iberian Pyrite Belt, Southern Portugal). Land Degradation Development 16,
825 213-228.
826 Ferreira da Silva, E., Patinha, C., Reis, P., Cardoso Fonseca, E., Matos, J.X., Barrosinho, J.,
827 Santos Oliveira, J.M., 2006. Interaction of acid mine drainage with waters and sediments at
828 the Corona stream, Lousal mine (Iberian Pyrite Belt, Southern Portugal).Environ. Geol. 50,
829 1001-1013.
830 Freeze, R.A., Cherry, J.A., 1979, Groundwater. Prentice-Hall, New Jersey.
831 Gammons, C.H., Wood, S.A., Jonas J.P., Madison J.P., 2003. Geochemistry of rare elements
832 and uranium in the acidic Berkeley Pit Lake, Butte, Montana. Chem. Geol.198, 269-288.
833 Gammons, C.H., Wood, S.A., Nimick D.A., 2005a. Diel behaviour of rare earth elements in a
834 mountain stream with acidic to neutral pH. Geochim. Cosmochim. Acta 69, 3747-3758.
835 Gammons, C.H., Wood, S.A., Pedrozo, F., Varekamp, J.C., Nelson, B.J., Shope, C.L., Baffico,
836 G., 2005b. Hydrogeochemistry and rare earth element behaviour in a volcanically acidified
837 watershead in Patagonia, Argentina. Chem. Geol. 222, 249-267.
838 Gimeno Serrano, M.J., 1999. Estudio del comportamiento geoquimico de las tierras rares en un
839 sistema natural de aquas acidas (Arroyo del Val-Badenas). PhD. Thesis, Univ. Zaragoza,
840 Spain.
841 Gimeno Serrano, M.J., Auqué, L.F., Nordstrom, D.K., 2000. REE speciation in low-temperature
842 acidic waters and the competitive effects of aluminium. Chem. Geol. 165, 167-180.
843 Goldstein, S.J., Jacobsen, S.B. 1988 Rare earth elements in river waters. Earth Planet. Sci.
844 Lett. 89, 35- 47.
845 Gosselin, D.C., Smith, M.R., Lepel, E.A., Lau, L.J.C., 1992. Rare earth elements in chloride-rich
846 groundwater, Palo Duro Basin, Texas, USA. Geochim. Cosmochim. Acta 56, 1495- 1505.
847 Grimes, D.J., Earhart, R.L., Carvalho, D., 1998. Rare earth element distribution in the volcanic
848 lithostratigraphic units of the Portuguese Pyrite Belt. In: Grimes, D.J., Kropschot , S.J.
849 (Eds), Geochemical Studies of Rare Earth Elements in the Portuguese Pyrite Belt, and
850 Geologic and Geochemical controls on Gold distribution. U.S. Geol. Surv. Prof. Paper 1596
851 A-B, Part A, 6-13.
852 Gromet, L.P., Dymek, R.F. Haskin, L.A., Korotev, R.L., 1984. The “North American shale
853 composite” its compilation,major, and trace elements characteristics. Geochim.
854 Cosmochim. Acta 48, 2469-2482.
855 Gruau G., Dia, A., Olivié-Lauquet, G., Davranche, M., Pinay, G., 2004. Controls on the
856 distribution of rare earth elements in shallow groundwater : New constraints from small
857 catchment Studies. Water Resour. 38, 3576-3586.
858 Haley, P.J., 1991. Pulmonary toxicity of stable and radioactive lanthanide. Health Phys. 61,
859 809–820.
860 Hirano, S., Suzuki, K.T., 1996. Exposure, metabolism and toxicity of rare earths and related
861 compounds. Environ. Health Perspectives 104 (Suppl. 1), 85–95.

Jambor, J.L., Nordstrom, D.K., Alpers, C.N., 2000. Metal-sulfate salts from sulfide mineral oxidation. In: Alpers, C.N., Jambor, J.L., Nordstrom, D.K. (Eds), Sulfate Minerals: Crystallography, Geochemistry, and Environmental Significance. Reviews in Mineralogy and Geochemistry 40, 303-350.

Jerz, J.K., Rimstidt, J.D., 2003. Efflorescent iron sulfate minerals: paragenesis, relative stability, and environmental impact. Am. Mineral, 88,1919-1932.

Johannesson, K.H., Lyons, W.B., 1995. Rare earth element geochemistry of Colour Lake, an acidic freshwater lake on Axel Heiberg Island, Norhwest Territories, Canada. Chem. Geol. 119, 209-223.

Johannesson, K.H., Zhou, X., 1999. Origin of middle rare earth element enrichments in acid waters of Canadian High Arctic Lake. Geochim. Cosmochim. Acta 63, 153-165.

Johannesson, K.H., Stetzenbach, K.J., Hodge, V.F., Lyons, W.B., 1996. Rare earth element complexation behavior in circumneutral pH groundwaters: Assessing the role of carbonate and phosphate ions. Earth Planet. Sci. Lett. 139, 305-319.

Karathanasis, A.D., Evangelou, V.P., Thompson, Y.L., 1988. Aluminium and iron equilibria in soil solutions and surface waters of acid mine watersheds. J. Environ. Quality 17, 534-543.

Kimball, B.A., 1999, Seasonal variation in metal concentrations in a stream affected by acid mine drainage, St. Kevin Gulch, Colorado. In Filipek, L. H., Plumlee, G. S. (Eds), The Environmental Geochemistry of Mineral Deposits - Part B, Case Studies and Research Topics. Littleton, Colorado, Society of Economic Geologists, 467-477.

Kimball, B.A., Bianchi, F., Walton-Day, K., Runkel, R.L., Nannucci, M., Salvadori, A., 2007, Quantification of changes in metal loading from storm runoff, Merse River (Tuscany, Italy). Mine Water Environment 26, 209-216.

Landa, E.R., Cravotta, C.A., Naftz, D.L., Verplanck, P.L., Nordstrom, D.K., Zielinski, R.A., 2000. Geochemical investigations by the USGS on uranium mining, milling and environmental restoration. Technology 7, 381-396.

Leybourne, M.I., Goodfellow, W.D., Boyle, D.R., 2000. Hydrogeochemical, isotopic and rare earth element geochemistry of acid-sulphate and acid-sulphate-chloride geothermal systems from Yellowstone National Park, Wyoming, USA. Geochim. Cosmochim. Acta 61, 695-723.

López-González, N., Borrego, J., de la Rosa, J., Grande, J.A., Carro, B., Lozano-Soria, O., 2005. Concentración y fraccionamiento de Tierras Raras en el agua del sistema fluvio-marino del rio Tinto (SO de España). Geogaceta 38, 151-154.

Ludwig, R., Ufer, K., Jochum, J., Friedrich, G., 2001. Pyrite oxidation in sediment samples from the German open-cut brown coal mine Zwenkau: mineral formation and dissolution of silicates. J. Plant Nutr. Soil Sci. 164, 283-288.

Marchand, E.A., 2002. Literature review. Minerals and Mine Drainage. Water Environment Res. 74 (5), 746-772.

Matos, J.X., 2005. Carta geológica e mineira da Mina do Lousal esc. 1/5000, INETI.

901 Matos, J.X., Martins, L., 2006. Reabilitação ambiental de áreas mineiras do sector português da
902 Faixa Piritosa Ibérica: estado da arte e perspectivas futuras. IGME, Boletín Geológico y
903 Minero España 117, 289-304.
904 Merten D., Geletneky J., Bergmann H., Haferburg G., Kothe E., Buchel G., 2005. Rare earth
905 element patterns: a tool for understanding processes in remediation of acid mine drainage.
906 Chemie der Erde Geochem. 5, 97-114.
907 Miekeley, N., Casartelli, E.A., Dotto, R.M., 1994. Concentration levels of rare-earth elements
908 and thorium in plants from Morro de Ferro environment as an indicator of the biological
909 availability of transuranium elements. J. Radioanal. Nucl. Chem. 182, 75-89.
910 Miekeley, N., Coutinho de Jesus, H., Porto da Silveira, C.L., Linsalata, P., Morse, R. 1992.
911 Rare-earth elements in ground waters from the Osamu Utsumi mine and Morro do Ferro
912 analogue study sites, Poços de Caldas, Brazil. J. Geochem. Explor. 45, 365-387.
913 Minarik L., Zigova A., Bendl J., Skrivan P., Stástny M., 1998. The behaviour of rare-earth
914 elements and Y during the rock weathering and soil formation in the Ricany granite massif,
915 central Bohemia. Sci. Total Environ. 215, 101-111.
916 Nagorski, S.A., Moore, J.N., McKinnon, T.E., Smith, D.B., 2003a, Geochemical response to
917 variable streamflow conditions in contaminated and uncontaminated streams. Water
918 Resour. Res. 39 (2), 1-14.
919 Nagorski, S.A., Moore, J.N., McKinnon, T.E., Smith, D.B., 2003b, Scale-dependent temporal
920 variations in stream water geochemistry: Environ. Sci. Technol. 37, 859-864.
921 Nasraoui, M., Toulkeridis, T., Clauer, N., Essaid Bilal, E., 2000. Differentiated hydrothermal and
922 meteoric alterations of the Lueshe carbonatite complex_Democratic Republic of Congo/
923 identified by a REE study combined with a sequential acid-leaching experiment. Chem.
924 Geol. 165, 109-132
925 Nesbitt, H.W. 1979. Mobility and fractionation of rare elements during weathering of a
926 granodiorite. Nature 279, 206-210.
927 Nordstrom, D.K., 1982. Aqueous pyrite oxidation and the consequent formation of secondary
928 iron minerals. In: Kittrick, J.A. (Ed.), Acid Sulfate Weathering. American Soil Science
929 Special Publication 10, 37–57.
930 Nordstrom, D.K., Alpers, C.N., 1999. Geochemistry of acid mine waters. Rev. Econ. Geol. 6(B),
931 133-160.
932 Nordstrom, D.K., Carlson-Foscz, V., Oreskes, N. 1995 Rare earth elements fractionation during
933 acid weathering of San Juan Tuff, Colorado. Ann. Meeting Geol. Soc. Am. Abstracts with
934 Program 27, A-199.
935 Nyakairu, G.W.A., Koeberl, C., Kurzweil, 2001. The Buwambo kaolin deposit in central Uganda:
936 Mineralogical and chemical composition. Geochem. J. 35, 245-256.
937 Olias, M, Cerón, J., Fernández, I., De la Rosa, I., 2005. Distribution of rare earth elements in an
938 alluvial aquifer affected by acid mine drainage: the Guadiamar aquifer (SW Spain) Environ.
939 Pollut. 135, 53-64.

940 Oliveira, J.M.S., Farinha, J., Matos, J.X., Ávila, P., Rosa, C., Machado, M.J.C., Daniel, F.S.,
941 Martins, L., Leite, M.R.M., 2002. Diagnóstico ambiental das principais áreas mineiras
942 degradadas do País. Boletim de Minas 30 (2), 67-85.
943 Oliveira, V.M.J., Matos, J.X., Rosa, C., 2001. The NNW sector of the Iberian Pyrite Belt – new
944 exploration perspectives for the next decade. Geode Workshop – Massive sulphide
945 deposits in the Iberian Pyrite Belt: new advances and comparison with equivalent systems,
946 Aracena Spain, 34-37.
947 Plumlee, G.S., Smith, K.S., Montour, M.R., Ficklin, W. H., Mosier, E.L., 1999. Geologic controls
948 on the composition of natural waters and mine waters draining diverse mineral deposit
949 types. Rev. Econ. Geol. 6(B), 373–407.
950 Protano, G., Riccobono, F., 2002. High contents of rare earth elements (REEs) in stream waters
951 of a Cu-Pb-Zn mining area. Environ. Pollut. 117, 499-514.
952 Ramsey, M.H., Thompson, M., Banerjee,E.K., 1987. Realistic assessment of analytical data
953 quality from inductively coupled plasma atomic emission spectrometry. Anal. Proc. 24, 260-
954 265.
955 Reimann, C., de Caritat, P., 1998. Chemical Elements in the Environment. Springer Verlag.
956 Ritsema, C.J., Groenenberg, J.E., 1993. Pyrite oxidation, carbonate weathering, and gypsum
957 formation in a drained potential acid sulfate soil. Soil Sci. Soc. Am. J. 57, 968–976.
958 Romero, A., González I., Galán E, 2006a. Estimation of potential pollution of waste mining
959 dumps at Pen˜a del Hierro (Pyrite Belt, SW Spain) as a base for future mitigation actions.
960 Appl. Geochem.21, 1093–1108.
961 Romero, A., González, I., Galán, E. 2006b. The role of efflorescent sulfates in the storage of
962 trace elements in stream waters polluted by acid mine-drainage: the case of Peña del
963 Hierro, southwestern Spain. Can. Mineral. 44, 1431-1446.
964 Sànchez-España, J., López Pamo, E., Santofimia, E., Aduvire, O., Reyes, J., Barettino, D.,
965 2005. Acid mine drainage in the Iberian Pyrite Belt Odiel river watershed, Huelva, SW
966 Spain): geochemistry, mineralogy and environmental implications. Appl. Geochem. 20,
967 1320-1356.
968 Sholkovitz, E.R., 1995. The aquatic geochemistry of rare earth elements in rivers and estuaries.
969 Aquat. Geochem. 1, 1-43.
970 Sholkovitz, E.R., Elderfield, H., Szymczak, R., Casey, K., 1999. Island weathering: river sources
971 of rare earth elements to the Western Pacific Ocean. Mar. Chem. 68, 39-57.
972 Smedley P.L., 1991. The geochemistry of rare earth elements in groundwater from the
973 Carnmenellis area, southwest England. Geochim. Cosmochim. Acta 55, 2767-2779.
974 Smith, K.S., 1999, Metal Sorption on Mineral Surfaces: An Overview with Examples Relating to
975 Mineral Deposits. In: Plumlee, G. S., Logsdon, M. J. (Eds), The Environmental
976 Geochemistry of Mineral Deposits Part A: Processes, Techniques, and Health Issues.
977 Littleton, Colorado, Society of Economic Geologists, 161-182.

978 Strauss, G., 1970. Sobre la geologia de la provincia piritífera del SW de la Península Ibérica y
979 de sus yacimientos, en especial sobre la mina de pirita de Lousal (Portugal). Memórias
980 Instituto Tecnológico GeoMinero España. 77.
981 Tabaksblat, L.S., 2002. Specific features in the formation of the mine water microelement
982 composition during ore mining. Water Resour. 29, 333-345.
983 Tornos, F., Barriga, F., Marcoux, E., Pascual, E., Pons, J.M., Relvas, J., Velasco, F., 2000. The
984 Iberian Pyrite Belt. In: Large R., Bloundell D. (Eds), GEODE database on global VMS
985 districts CODES SRC, Tasmania, 19-52.
986 Verplanck P.L., Nordstrom D.K., Gimeno M.J., Wright WG. 1999. Rare earth element
987 geochemistry of natural and mining-related acid waters, Upper Animas River basin,
988 Colorado. 7th Ann.l V. M. Goldschmidt Conf., 2417.
989 Verplanck, P.L., Nordstrom, D.K., Taylor, H.E., Kimball, B.A., 2004. Rare earth element
990 partitioning between hydrous ferric oxides and acid mine water during iron oxidation. Appl.
991 Geochem. 19, 1339-1354.
992 Wan, Y., Liu, C., 2006. The effect of humic acid on the adsorption of REE on kaolin. Colloids
993 Surfaces A: Physicochem. Engin. Aspects 290, 112-117.
994 Wood, S.A., Gammons C.H., Parker, S.R., 2006. The behaviour or rare earth elements in
995 naturally and anthropogenically acidified waters. J. Alloys Compounds 418, 161-165.
996 Worrall F., Pearson D.G., 2001. Water-rock interaction in an acidic mine discharge as indicated
997 by rare earth element patterns. Geochim. Cosmochim. Acta 65, 3027-3040.
998 Zhao, F., Cong, Z., Sun, H., Ren, D., 2007. The geochemistry of rare earth elements (REE) in
999 acid mine drainage from the Sitai coal mine, Shanxi Province, North China, Internat. J. Coal
1000 Geol. 70, 184-192.

Figure Captions

Fig. 1. (a) The NNW Sector of the Iberian Pyrite Belt (adapted from Oliveira et al. 2001) (b) Lousal Mine region simplified geological map: 1 – Acid water lagoons; 2 - Acid mine drainage; 3 – Mine waste/contaminated landfill; 4 - Undifferentiated Tertiary Sado Basin and Quaternary alluvionar sediments; Palaeozoic Basement (South Portuguese Zone): 5 - Mértola Fm. (Late Visean); Volcano-Sedimentary Complex (Late Devonian-Late Visean): 6 – VSC sediments; 7 – Massive sulfide ore (Lousal gossans); 8 - VSC volcanics; Phyllite-Quartzite Group (Late Devonian): 9 – Corona Fm. shales and quartzites. 10 – Thrust fault; 11 – Strike-slip fault; 12 – Geological limit. 13 – Sampling site; 14 – AMD source; 15 – Stream; 16 – Railway [ad. Matos 2005, Oliveira et al., 2002]; c) Lousal 3D map showing the abandoned mining area (from http://maps.live.com); T_A and T_B – tailings piles.

Fig. 2. Binary plots of (a and b) pH versus SO_4^{2-}, Fe and Al, (c and d) SO_4^{2-} versus Zn, Ni and La, (e) Zn versus Cd, (f) Ni versus Co concentrations in the acidic waters (AMW1, AMW2, AMW18, AMW19), impacted Corona stream waters (SW6, SW8, SW9, SW12) and background surface water samples (SW3, SW4, SW10, SW14).

Fig. 3. Ficklin diagram corresponding to water samples collected from Lousal area. (a) Sample label 1 represents the mine lagoon water sample (AMW1), sample label 2 represents the spring water (AMW 2), sample labels 18 and 19 represent the flowing channel waters from the tailings piles (AMW18 and AMW19), and (b) sample labels 6, 8, 9, 12 represent the water samples from the impacted Corona stream (SW6, SW8, SW9, SW12), sample label 14 represents the Sado river sample (SW14), and sample label 10 the water sample from Lousal stream (SW10). (c) Plot showing the spatial changes of REE and pH values along the Corona stream.

Fig. 4. Scanning electron microscopy images of natrojarosite (a), coquimbite (b and e), Mg-copiapite (c) and Al-copiapite (e), alunite and gypsum (d), halotrickite + pickeringite (f).

Fig. 5. The NASC normalized distributions of REE of the VMS host rocks and pyrite ore. Abbreviations: BSPy - black shales with pyrite; BS - black shales; SP - spilitic rock; K - kaolin rock; MPy - pyrite.

Fig. 6. The NASC normalized REE distribution patterns of acidic mine waters. (a) (▲) AMW1 – Open-pit lake and (■) AMW2 - acid spring; (b): (✱) AMW18 - seeps from tailings T_A and (●) AMW19 - seeps from tailings T_B. (light gray – winter; dark gray – spring; black – summer).

Fig. 7. The NASC normalized REE distribution patterns of efflorescent sulfates formed in the Corona stream. (a) EF3 – Szomolnokite; EF7 and EF8 – Gypsum, rozenite, alunite, kaolinite; EF9 – Schwertmanite; (b) EF1 – Hexahidrite; EF2 – Rozenite, Alunite; EF4 – Rozenite, Alunite, Gypsum, Halotrichite; EF5 – Rozenite, Alunite, Gypsum; EF6 – Copiapite, Coquimbite.

Fig. 8. The NASC normalized REE distribution patterns of stream waters in winter (a), spring (b) and summer (c). Abbreviations: SW6 (+), SW8 (■), SW9 (▲), SW12 (◆) – Corona stream. Samples SW10 (Lousal stream) and SW14 (Sado river) are not plotted because the REE concentrations are below the detection limits.

Fig. 9. The NASC normalized REE distribution patterns of the streambed sediment samples of the Corona stream - SS3 (▲), SS4 **(▼)**, SS6 (●), SS8 (✱), SS9 (◆), SS12 (♦) Lousal stream - SS10 (+) and Sado river - SS14(■).

Table captions

Table 1. Chemical composition of host rock and pyrite samples collected at the Lousal area (*mean values of 3 samples).

Table 2. Trace element concentrations determined in the Corona, Lousal and Sado stream sediment samples.

Table 3. Values of field parameters and, trace elements and REE concentrations of the acidic mine water samples.

Table 4. The seasonal distribution of ΣLREE, ΣHREE, ΣREE, ΣLREE/ΣHREE, Ce/Ce* and Eu/Eu*anomalies, and normalized concentration ratios of $(La/Yb)_N$ and $(Sm/Nd)_N$ in the acidic mine waters.

Table 5a. Physical parameters, REE concentrations, and other selected variables (winter) and distribution of ΣLREE, ΣHREE, ΣREE, ΣLREE/ΣHREE, Ce/Ce* and Eu/Eu*anomalies, and normalized concentration ratios of $(La/Yb)_N$ and $(Sm/Nd)_N$ in the surface water samples from the Corona stream.

Table 5b. Physical parameters, REE concentrations, and other selected variables (spring) and distribution of ΣLREE, ΣHREE, ΣREE, ΣLREE/ΣHREE, Ce/Ce* and Eu/Eu* anomalies, and normalized concentration ratios of $(La/Yb)_N$ and $(Sm/Nd)_N$ in the surface water samples from the Corona stream.

Table5c. Physical parameters, REE concentrations, and other selected variables (summer) and distribution of ΣLREE, ΣHREE, ΣREE, ΣLREE/ΣHREE, Ce/Ce* and Eu/Eu* anomalies, and normalized concentration ratios of $(La/Yb)_N$ and $(Sm/Nd)_N$ in the surface water samples from the Corona stream.

Table 6. Chemical composition of efflorescent sulfates sampled in the Corona stream and distribution of ΣLREE, ΣHREE, ΣREE, ΣLREE/ΣHREE, Ce/Ce* and Eu/Eu* anomalies, and normalized concentration ratios of $(La/Yb)_N$ and $(Sm/Nd)_N$.

Table 1
Chemical composition of host rock and pyrite samples collected at Lousal area (*mean values of 3 samples).

		host rock samples*				Pyrite ore*
		BS	**SP**	**K**	**BSPy**	**MPy**
Ag	mg kg^{-1}	0.3	0.1	b.d.l.	24.0	43.2
As	mg kg^{-1}	55	8	115	1341	12576
Bi	mg kg^{-1}	5	0.1	0.1	33.1	56.6
Cd	mg kg^{-1}	0.4	0.2	0.1	18.2	1.0
Co	mg kg^{-1}	6	49	13	7	159
Cu	mg kg^{-1}	80	61	642	767	7629
Mo	mg kg^{-1}	0.7	0.6	0.4	0.2	0.9
Ni	mg kg^{-1}	2	123	20	6	34
Pb	mg kg^{-1}	50	11	3	9908	14009
Sb	mg kg^{-1}	9.7	0.1	10.3	210	760
Zn	mg kg^{-1}	199	78	132	8651	237
La	mg kg^{-1}	9.80	11.0	15.5	3.30	0.50
Ce	mg kg^{-1}	20.8	26.8	35.3	3.60	0.50
Pr	mg kg^{-1}	2.31	3.18	4.63	0.65	0.03
Nd	mg kg^{-1}	9.50	15.0	22.3	2.40	0.40
Sm	mg kg^{-1}	1.50	3.50	5.90	0.50	0.10
Eu	mg kg^{-1}	0.48	1.28	1.66	0.50	b.d.l.
Gd	mg kg^{-1}	1.36	3.55	4.59	0.32	b.d.l.
Tb	mg kg^{-1}	0.28	0.59	0.66	0.08	b.d.l.
Dy	mg kg^{-1}	1.92	3.03	3.18	0.47	b.d.l.
Ho	mg kg^{-1}	0.38	0.69	0.56	0.12	b.d.l.
Er	mg kg^{-1}	1.05	1.64	1.56	0.25	b.d.l.
Tm	mg kg^{-1}	0.15	0.23	0.26	0.05	b.d.l.
Yb	mg kg^{-1}	1.04	1.52	1.63	0.33	b.d.l.
Lu	mg kg^{-1}	0.14	0.22	0.23	0.04	b.d.l.
ΣLREE	mg kg^{-1}	43.9	59.5	83.6	10.5	1.53
ΣHREE	mg kg^{-1}	6.80	12.8	14.3	2.16	0
ΣREE	mg kg^{-1}	50.7	72.3	97.9	12.61	1.53
Ratio	-	6.46	4.67	5.84	4.84	-
Ce/Ce*	-	0.99	1.03	0.95	0.56	0.93
Eu/Eu*	-	1.48	1.60	1.40	5.49	-
$(La/Yb)_N$	-	0.91	0.70	0.92	0.97	-
$(La/Gd)_N$	-	1.17	0.50	0.55	1.67	-

Abbreviations: MPy-massive pyrite; BSPy-black shales with disseminated pyrite; BS-black shales; SP-spilitic rock; K-kaolin; MPy – pyrite; b.d.l. (below detection limit); Light REE (LREE: La to Sm); Heavy REE (HREE: Eu to Lu); ΣLREE= Sum of total concentration of Rare Earth elements; Ratio = ΣLREE/ΣHREE; Ce/Ce*= the value of the Ce anomaly calculated by the formula $Ce/Ce^* = [(Ce_N)/(SQR(La_N*Pr_N))]$ from Worrall and Pearson, 2001; Eu/Eu*= the value of the Eu anomaly calculated by the formula $[Eu/Eu^*]=[(Eu_N)/(SQR(Sm_N*Gd_N))]$ from Worrall and Pearson, 2001. Eu_N, Sm_N, Gd_N = shale-normalized values against NASC (Gromet et al., 1984); $(La/Gd)_N$ and $(La/Yb)_N$ are normalized concentration ratios in the selected samples.

Table 2
Trace element concentrations determined in the Corona, Lousal and Sado stream sediments samples.

Location		**Corona stream**						**Sado river**	**Lousal stream**
Nº		**SS3**	**SS 4**	**SS6**	**SS8**	**SS9**	**SS12**	**SS14**	**SS10**
Type		**Background**		**-------Impacted stream by AMD-------**					
Distance(m)				**100[(a)]**	**1030[(a)]**	**2325[(a)]**	**4725[(a)]**	**5700[(a)]**	
Ag	mg kg^{-1}	0.2	0.1	21.7	1.7	0.6	1.5	0.3	0.1
As	mg kg^{-1}	28	9	278	557	435	670	94	26
Bi	mg kg^{-1}	0.6	0.3	146.9	17.6	5.6	14.9	3.2	0.4
Cd	mg kg^{-1}	0.2	0.2	5.6	1.0	0.5	0.8	5.7	0.1
Co	mg kg^{-1}	11	9	40	45	17	29	73	23
Cu	mg kg^{-1}	21	19	1588	557	346	442	597	28
Mo	mg kg^{-1}	0.3	0.2	5.6	1.1	0.6	1.1	0.5	0.7
Ni	mg kg^{-1}	21	23	20	17	8	17	45	41
Pb	mg kg^{-1}	91	39	8523	834	285	664	149	36
Sb	mg kg^{-1}	3.5	1.4	138.1	34.5	13.8	25.7	5.0	1.6
Zn	mg kg^{-1}	65	57	2756	627	385	456	2398	114
La	mg kg^{-1}	23.9	23.7	34.8	19.1	21.1	19.6	33.7	27.5
Ce	mg kg^{-1}	52.1	50.2	78.7	40.0	44.9	41.8	78.3	63.3
Pr	mg kg^{-1}	6.12	6.05	8,88	4.76	5.44	4.85	9.32	6.91
Nd	mg kg^{-1}	23.8	24.3	34.4	18.0	20.9	19.3	38.7	27.9
Sm	mg kg^{-1}	4.50	4.50	6.70	3.40	3.90	3.90	7.50	5.30
Eu	mg kg^{-1}	0.89	0.88	1.41	0.69	0.78	0.75	1.57	1.14
Gd	mg kg^{-1}	3.93	3.85	5.92	3.03	3.22	3.52	6.48	4.56
Tb	mg kg^{-1}	0.65	0.58	0.86	0.48	0.56	0.67	1.08	0.88
Dy	mg kg^{-1}	3.38	3.31	5.15	2.99	3.07	3.82	5.75	4.65
Ho	mg kg^{-1}	0.63	0.63	0.91	0.54	0.62	0.74	0.96	0.83
Er	mg kg^{-1}	1.94	1.93	2.61	1.66	2.01	2.42	2.89	2.67
Tm	mg kg^{-1}	0.29	0.27	0.41	0.25	0.31	0.38	0.43	0.42
Yb	mg kg^{-1}	1.96	1.88	2.71	1.73	2.16	2.28	2.88	2.77
Lu	mg kg^{-1}	0.28	0.29	0.38	0.24	0.31	0.34	0.40	0.37
ΣLREE	mg kg^{-1}	110.4	108.8	163.5	85.3	96.2	89.5	167.5	130.9
ΣHREE	mg kg^{-1}	13.9	13.6	20.4	11.6	13.0	14.9	22.4	18.3
ΣREE	mg kg^{-1}	124.3	122.4	183.9	96.9	109.2	104.4	189.9	149.2
Ratio	-	7.93	7.98	8.03	7.34	7.38	6.00	7.47	7.16
Ce/Ce*	-	0.98	0.95	1.02	0.95	0.95	0.97	1.00	1.04
Eu/Eu*	-	0.93	0.93	0.98	0.95	0.97	0.89	0.99	1.02
$(La/Yb)_N$	-	1.18	1.22	1.24	1.07	0.95	0.83	1.13	0.96
$(La/Gd)_N$	-	0.99	1.00	0.96	1.03	1.07	0.91	0.85	0.98

Abbreviations: SS3, SS4, SS6, SS8, SS9, SS12 – samples from Corona stream; SS10 – sample from Lousal stream; SS14 – sample from Sado river; (a) distance from the open pit; b.d.l. (below detection limit); Light REE (LREE: La to Sm); Heavy REE (HREE: Eu to Lu); ΣLREE= Sum of total concentration of Rare Earth elements; Ratio = ΣLREE/ΣHREE; Ce/Ce*= the value of the Ce anomaly calculated by the formula Ce/Ce* = [(Ce_N)/(SQR(La_N*Pr_N))] from Worrall and Pearson, 2001; Eu/Eu*= the value of the Eu anomaly calculated by the formula [Eu/Eu*]=[(Eu_N)/(SQR(Sm_N*Gd_N))] from))] from Worrall and Pearson, 2001. Eu_N, Sm_N, Gd_N = shale-normalized values against NASC (Gromet et al., 1984); $(La/Gd)_N$ and $(La/Yb)_N$ are normalized concentration ratios in the selected samples

Table 3
Values of field parameters and, trace elements and REE concentrations of the acidic mine water samples.

Var	Units	AMW1	AMW2	AMW18	AMW19
T	ºC	16.4-20.6	18.4-24.5	18.2-25.7	15.1-21.5
pH	-	2.9 - 3.0	2.7-2.8	1.9-2.0	2.0-2.3
EC	mS cm^{-1}	4.85-6.60	5.73-9.30	10.62-24.00	6.25-7.85
SO_4^{2-}	mg/L	4635-5040	4899-11610	8019-20070	7530-9240
Cl	mg/L	60-151	46-313	1-57	1-19
Ag	µg L^{-1}	0.05-0.54	0.05-0.78	0.3-0.88	0.4-0.11
Al	mg L^{-1}	22.1-26.2	95.5-136	624-1100	327-430
As	µg L^{-1}	b.d.l.	2-95	21064-36455	4574-9000
Bi	µg L^{-1}	b.d.l.	0.05-0.15	14.27-26.31	0.05-0.09
Cd	µg L^{-1}	127-181	128-295	180-560	198-300
Co	µg L^{-1}	2529-3868	2109-5281	1770-6499	1549-3098
Cu	mg L^{-1}	7-11	9-12	23-111	29-50
Fe	mg L^{-1}	14.5-22.5	395-959	2250-8215	1526-1629
Mn	mg L^{-1}	122 - 129	102-224	38-49	14-38
Mo	µg L^{-1}	0.3-0.8	0.3-1.3	4.0-9.6	0.1-0.2
Ni	µg L^{-1}	1082-1627	1194-2007	964-1349	455-1349
Pb	µg L^{-1}	143-197	75-306	177-302	b.d.l.
Sb	µg L^{-1}	b.d.l.	b.d.l.	31-130	0.68-1.1
Zn	mg L^{-1}	66-77	90-170	199-269	130-219
La	µg L^{-1}	47.32-86.24	126.15-485.97	37.33-161.37	36.8-103.50
Ce	µg L^{-1}	132.49-164.12	354.44-849.99	137.97-295.01	159.73-224.09
Pr	µg L^{-1}	11.45-22.96	29.95-141.55	13.19-56.53	11.97-38.92
Nd	µg L^{-1}	80.64-106.75	215.99-655.30	95.34-283.72	83.72-168.88
Sm	µg L^{-1}	19.04-28.87	49.97-180.34	22.81-77.23	17.29-49.20
Eu	µg L^{-1}	3.01-5.56	5.84-23.70	7.58-32.62	4.70-19.47
Gd	µg L^{-1}	20.30-36.68	43.12-186.72	15.69-69.67	11.28-51.81
Tb	µg L^{-1}	3.86-7.20	7.59-34.46	2.82-12.62	1.86-9.64
Dy	µg L^{-1}	16.65-31.04	31.48-149.45	11.82-54.26	7.97-38.82
Ho	µg L^{-1}	3.42-6.15	6.06-27.51	2.23-10.08	1.53-7.28
Er	µg L^{-1}	7.89-14.68	13.69-64.32	5.47-26.31	3.86-18.12
Tm	µg L^{-1}	0.88-1.65	1.59-7.34	0.72-3.48	0.52-2.34
Yb	µg L^{-1}	4.37-7.86	8.16-35.1	4.53-20.82	3.22-15.05
Lu	µg L^{-1}	0.58-1.04	1.02-4.32	0.58-2.70	0.42-1.92

Abbreviations: AMW1-Open pit lagoon; AMW2 – Acidic Spring; AMW18 - Flowing channels from tailings A; AMW19 - Flowing channels from tailings B (data only for Winter and Spring seasons); EC – electric conductivity; b.d.l. – below detection limit.

Table 4

Table 4
The seasonal distribution of ΣLREE, ΣHREE, ΣREE, ΣLREE/ΣHREE, Ce/Ce* and Eu/Eu*anomalies, and normalized concentration ratios of $(La/Yb)_N$ and $(Sm/Nd)_N$ in the acidic mine waters.

		ΣLREE	ΣHREE	ΣREE	Ratio	Ce/Ce*	Eu/Eu*	$(La/Yb)_N$	$(La/Gd)_N$
Winter	AMW1	311.0	61.0	372.0	5.10	1.49	0.67	1.05	0.38
	AMW2	776.5	118.6	895.1	6.55	1.31	0.55	1.50	0.48
	AMW18	306.6	51.4	358.0	5.96	1.41	1.76	0.80	0.39
	AMW19	309.5	35.4	344.9	8.75	1.73	1.48	1.11	0.53
Spring	AMW1	377.3	111.9	489.2	3.37	0.68	0.75	1.06	0.38
	AMW2	2313.2	532.9	2846.1	4.34	0.74	0.57	1.34	0.42
	AMW18	873.9	232.6	1106.5	3.76	0.70	1.95	0.75	0.38
	AMW19	474.2	89.5	563.7	5.30	0.84	1.56	0.98	0.50
Summer	AMW1	380.1	100.6	480.7	3.78	0.89	0.74	1.14	0.38
	AMW2	1557.2	349.0	1906.2	4.46	0.84	0.60	1.37	0.38
	AMW18	584.6	164.5	749.1	3.55	0.81	1.69	0.67	0.33
	AMW19	ndt	ndt	ndt	-	-	-	-	-

Abbreviations: AMW1 - Open pit lagoon; AMW2 - Acid Spring; AMW18 - Flowing channels from tailings A; AMW19 - Flowing channels from tailings B. ndt – not determinated. Light REE (LREE: La to Sm); Heavy REE (HREE: Eu to Lu); ΣLREE= Sum of total concentration of Rare Earth elements; Ratio = ΣLREE/ΣHREE; Ce/Ce*= the value of the Ce anomaly calculated by the formula $Ce/Ce^* = [(Ce_N)/(SQR(La_N*Pr_N))]$ from Worrall and Pearson, 2001; Eu/Eu*= the value of Eu anomaly calculated by the formula $[Eu/Eu^*]=[(Eu_N)/(SQR(Sm_N*Gd_N))]$ from Worrall and Pearson, 2001. Eu_N, Sm_N, Gd_N = shale-normalized values against NASC (Gromet et al., 1984); $(La/Gd)_N$ and $(La/Yb)_N$ are normalized concentration ratios in the selected samples.

Table 5a

Physical parameters, REE concentrations, and others selected variables (winter) and distribution of ΣLREE, ΣHREE, ΣREE, ΣLREE/ΣHREE, Ce/Ce* and Eu/Eu*anomalies, and normalized concentration ratios of $(La/Yb)_N$ and $(Sm/Nd)_N$ in the surface water samples from the Corona stream.

Season	Stream		Corona stream						Sado	Lousal
	Type		Background		Impacted stream by AMD					Back
	Variables		SW3	SW4	SW6	SW8	SW9	SW12	SW14	SW10
	Distance				100	1030	2325	4725	5700	
Winter	T	ºC	20	21	18	19	20	19	17	19
	pH		7.5	7.4	7.3	6.8	6.9	7.3	7.5	7.6
	EC	µS cm^{-1}	520	488	497	511	495	503	1365	583
	SO_4^{2-}	mg L^{-1}	48	41	50	77	71	64	91	43
	Cl	mg L^{-1}	44	39	39	41	40	43	157	53
	Ag	µg L^{-1}	b.d.l.	b.d.l.	b.d.l.	b.d.l.	b.d.l.	b.d.l.	b.d.l.	b.d.l.
	Al	µg L^{-1}	158	188	489	693	1077	685	666	31
	As	µg L^{-1}	b.d.l.	b.d.l.	b.d.l.	b.d.l.	b.d.l.	b.d.l.	b.d.l.	b.d.l.
	Bi	µg L^{-1}	b.d.l.	b.d.l.	b.d.l.	b.d.l.	b.d.l.	b.d.l.	b.d.l.	b.d.l.
	Cd	µg L^{-1}	0.1	b.d.l.	0.3	1.2	1.0	0.6	0.5	b.d.l.
	Co	µg L^{-1}	2	1	5	14	12	9	3	b.d.l.
	Cu	µg L^{-1}	6	6	14	118	108	52	21	2
	Fe	µg L^{-1}	658	642	947	4485	4810	2623	1628	233
	Mo	µg L^{-1}	242	219	358	487	464	358	425	127
	Ni	µg L^{-1}	1	b.d.l.	2	4	4	3	b.d.l.	b.d.l.
	Pb	µg L^{-1}	b.d.l.	b.d.l.	b.d.l.	7	11	7	5	b.d.l.
	Sb	µg L^{-1}	b.d.l.	b.d.l.	b.d.l.	0.5	0.5	0.3	0.2	0.2
	Zn	µg L^{-1}	60	14	218	730	615	315	277	13
	La	µg L^{-1}	0.14	0.19	0.42	0.38	0.55	0.38	0.90	0.02
	Ce	µg L^{-1}	0.37	0.50	1.12	1.07	1.55	1.07	2.49	0.08
	Pr	µg L^{-1}	0.04	0.04	0.11	0.10	0.15	0.10	0.21	b.d.l.
	Nd	µg L^{-1}	0.27	0.29	0.78	0.76	1.07	0.75	1.30	0.04
	Sm	µg L^{-1}	b.d.l.	b.d.l.	0.16	0.17	0.25	0.15	0.25	b.d.l.
	Eu	µg L^{-1}	b.d.l.	b.d.l.	0.02	0.02	0.03	0.02	0.04	b.d.l.
	Gd	µg L^{-1}	0.02	0.02	0.12	0.13	0.19	0.13	0.14	b.d.l.
	Tb	µg L^{-1}	b.d.l.	b.d.l.	0.02	0.02	0.03	0.02	0.02	b.d.l.
	Dy	µg L^{-1}	0.03	b.d.l.	0.10	0.10	0.14	0.10	0.12	b.d.l.
	Ho	µg L^{-1}	b.d.l.	b.d.l.	b.d.l.	0.02	0.03	b.d.l.	0.02	b.d.l.
	Er	µg L^{-1}	b.d.l.	b.d.l.	0.04	0.04	0.06	0.04	0.05	b.d.l.
	Tm	µg L^{-1}	b.d.l.	b.d.l.	b.d.l.	b.d.l.	b.d.l.	b.d.l.	b.d.l	b.d.l.
	Yb	µg L^{-1}	b.d.l.	b.d.l.	0.02	0.03	0.04	0.03	0.04	b.d.l.
	Lu	µg L^{-1}	b.d.l.	b.d.l.	b.d.l.	b.d.l.	b.d.l.	b.d.l.	b.d.l	b.d.l.
	ΣLREE	µg L^{-1}	0.82	1.02	2.61	2.5	3.6	2.47	5.19	0.14
	ΣHREE	µg L^{-1}	0.05	0.02	0.3	0.34	0.49	0.32	0.39	b.d.l.
	ΣREE	µg L^{-1}	0.87	1.04	2.91	2.84	4.09	2.79	5.58	0.14
	Ratio	-	16.4	51	8.7	7.35	7.34	7.72	13.31	n.d.t
	Ce/Ce*	-	1.12	1.30	1.18	1.25	1.23	1.25	1.30	n.d.t
	Eu/Eu*	-	n.d.t	n.d.t	0.63	0.59	0.60	0.63	0.94	n.d.t
	$(La/Yb)_N$	-	n.d.t	n.d.t	2.03	1.23	1.33	1.23	2.18	n.d.t
	$(La/Gd)_N$	-	1.14	1.55	0.57	0.48	0.47	0.48	1.05	n.d.t

EC – electric conductivity; b.d.l. – below detection limit. n.a. – not analysed because the stream was dry; n.d.t. – not determined. Ce/Ce*= the value of the Ce anomaly calculated by the formula $Ce/Ce^* = [(Ce_N)/(SQR(La_N*Pr_N))]$ from Worrall and Pearson, 2001; Eu/Eu*= the value of the Eu anomaly calculated by the formula $[Eu/Eu^*]=[(Eu_N)/(SQR(Sm_N*Gd_N))]$ from Worrall and Pearson, 2001. Eu_N, Sm_N, Gd_N = shale-normalized values

against NASC (Gromet et al., 1984). Abbreviations: SW3, SW4, SW6, SW8, SW9, SW12 – samples from Corona stream; SW10 – sample from Lousal stream; SW14 – sample from Sado river.

Table 5b
Physical parameters, REE concentrations, and others selected variables (spring) and distribution of ΣLREE, ΣHREE, ΣREE, ΣLREE/ΣHREE, Ce/Ce* and Eu/Eu*anomalies, and normalized concentration ratios of $(La/Yb)_N$ and $(Sm/Nd)_N$ in the surface water samples from the Corona stream.

Season	Stream		Corona stream						Sado	Lousal
	Type		Background		Impacted stream by AMD					Back
	Variables		SW3	SW4	SW6	SW8	SW9	SW12	SW14	SW10
	Distance				100	1030	2325	4725	5700	
Spring	T	ºC	14	14	16	18	17	16	16	17
	pH		7.3	7.2	6.4	3.3	2.8	3.1	6.0	7.1
	EC	µS cm^{-1}	870	760	930	1240	1621	1284	1173	486
	SO_4^{2-}	mg L^{-1}	53	43	196	528	808	553	200	44
	Cl	mg L^{-1}	174	139	152	143	131	126	226	83
	Ag	µg L^{-1}	b.d.l.	b.d.l.	b.d.l.	b.d.l.	b.d.l.	b.d.l.	b.d.l.	b.d.l.
	Al	µg L^{-1}	90	69	3460	10272	27000	12001	56	20
	As	µg L^{-1}	b.d.l.	b.d.l.	b.d.l.	b.d.l.	5	b.d.l.	b.d.l.	b.d.l.
	Bi	µg L^{-1}	b.d.l.	b.d.l.	b.d.l.	b.d.l.	b.d.l.	b.d.l.	b.d.l.	b.d.l.
	Cd	µg L^{-1}	b.d.l.	b.d.l.	4.8	17.1	30.1	19.6	4.1	b.d.l.
	Co	µg L^{-1}	2	1	95	216	321	250	64	0.2
	Cu	µg L^{-1}	5	3	225	2219	4717	2903	45	4
	Fe	µg L^{-1}	853	638	8254	7422	61600	12111	57	180
	Mo	µg L^{-1}	b.d.l.	b.d.l.	0.2	b.d.l.	b.d.l.	b.d.l.	b.d.l.	b.d.l.
	Ni	µg L^{-1}	b.d.l.	b.d.l.	32	51	70	56	14	b.d.l.
	Pb	µg L^{-1}	b.d.l.	b.d.l.	3	116	492	287	b.d.l.	b.d.l.
	Sb	µg L^{-1}	0.1	0.2	0.3	b.d.l.	0.1	b.d.l.	0.1	0.1
	Zn	µg L^{-1}	33	12	2397	7276	12709	8474	2090	30
	La	µg L^{-1}	0.36	0.31	9.07	6.10	10.14	9.56	b.d.l.	b.d.l.
	Ce	µg L^{-1}	0.60	0.52	16.2	11.0	20.1	17.8	0.04	b.d.l.
	Pr	µg L^{-1}	0.08	0.08	2.70	1.36	3.71	3.07	b.d.l.	b.d.l.
	Nd	µg L^{-1}	0.38	0.35	13.0	9.78	17.8	14.2	0.02	b.d.l.
	Sm	µg L^{-1}	0.09	0.07	3.42	2.61	4.73	3.73	b.d.l.	b.d.l.
	Eu	µg L^{-1}	b.d.l.	b.d.l.	0.52	0.73	1.39	0.95	b.d.l.	b.d.l.
	Gd	µg L^{-1}	0.08	0.05	3.57	2.59	4.37	3.54	0.01	b.d.l.
	Tb	µg L^{-1}	b.d.l.	b.d.l.	0.66	0.47	0.79	0.65	b.d.l.	b.d.l.
	Dy	µg L^{-1}	0.05	0.02	2.75	2.00	3.32	2.72	b.d.l.	b.d.l.
	Ho	µg L^{-1}	b.d.l.	b.d.l.	0.51	0.37	0.63	0.52	b.d.l.	b.d.l.
	Er	µg L^{-1}	0.02	b.d.l.	1.21	0.91	1.55	1.28	b.d.l.	b.d.l.
	Tm	µg L^{-1}	b.d.l.	b.d.l.	0.14	0.10	0.20	0.16	b.d.l.	b.d.l.
	Yb	µg L^{-1}	b.d.l.	b.d.l.	0.71	0.61	1.13	0.88	b.d.l.	b.d.l.
	Lu	µg L^{-1}	b.d.l.	b.d.l.	0.09	0.08	0.15	0.11	b.d.l.	b.d.l.
	ΣLREE	µg L^{-1}	1.51	1.33	44.4	30.9	56.4	48.4	0.06	b.d.l.
	ΣHREE	µg L^{-1}	0.15	0.07	10.2	7.86	13.5	10.8	0.01	b.d.l.
	ΣREE	µg L^{-1}	1.66	1.40	54.6	38.7	69.9	59.2	0.07	b.d.l.
	Ratio	-	10.07	19.00	4.37	3.93	4.17	4.47	6.00	n.d.t
	Ce/Ce*	-	0.80	0.75	0.75	0.87	0.74	0.75	n.d.t	n.d.t
	Eu/Eu*	-	n.d.t	n.d.t	0.65	1.23	1.34	1.15	n.d.t	n.d.t
	$(La/Yb)_N$	-	n.d.t	n.d.t	1.24	0.97	0.87	1.05	n.d.t	n.d.t
	$(La/Gd)_N$	-	0.73	1.01	0.41	0.38	0.38	0.44	n.d.t	n.d.t

EC – electric conductivity; b.d.l. – below detection limit; n.d.t. – not determined. Ce/Ce*= the Ce anomaly calculated by the formula $Ce/Ce^* = [(Ce_N)/(SQR(La_N*Pr_N))]$ from Worrall and Pearson, 2001; Eu/Eu*= the Eu anomaly calculated by the formula $[Eu/Eu^*]=[(Eu_N)/(SQR(Sm_N*Gd_N))]$ from Worrall and Pearson, 2001. Eu_N, Sm_N, Gd_N = shale-normalized values against NASC (Gromet et al., 1984). Abbreviations: SW3, SW4, SW6,

SW8, SW9, SW12 – samples from Corona stream; SW10 – sample from Lousal stream; SW14 – sample from Sado river.

Table 5c

Table5c

Physical parameters, REE concentrations, and others selected variables (summer) and distribution of ΣLREE, ΣHREE, ΣREE, ΣLREE/ΣHREE, Ce/Ce* and Eu/Eu*anomalies, and normalized concentration ratios of $(La/Yb)_N$ and $(Sm/Nd)_N$ in the surface water samples from the Corona stream.

Season	Stream		Corona stream						Sado	Lousal
	Type		Background		Impacted stream by AMD					Back
	Variables		SW3	SW4	SW6	SW8	SW9	SW12	SW14	SW10
	Distance				100	1030	2325	4725	5700	
Summer	T	ºC	28	27	31	28	28	27	26	(a)
	pH		6.9	7.8	4.0	3.4	3.2	6.6	8.1	(a)
	EC	µS cm^{-1}	1179	1030	2.18*	1818	2.53*	1362	1408	(a)
	SO_4^{2-}	mg L^{-1}	24	43	1221	1306	728	460	131	(a)
	Cl	mg L^{-1}	153	139	144	154	129	125	220	(a)
	Ag	µg L^{-1}	0.15	0.07	0.19	0.29	0.24	0.36	0.26	(a)
	Al	µg L^{-1}	799	122	35409	32000	11361	1013	1515	(a)
	As	µg L^{-1}	14	11	4	4	4	13	9	(a)
	Bi	µg L^{-1}	b.d.l.	b.d.l.	b.d.l.	b.d.l.	b.d.l.	b.d.l.	b.d.l.	(a)
	Cd	µg L^{-1}	0.9	0.1	53.4	49.9	28.6	2.6	1.0	(a)
	Co	µg L^{-1}	19	3	910	774	421	48	17	(a)
	Cu	µg L^{-1}	50	9	2446	3128	1955	20	62	(a)
	Fe	µg L^{-1}	7380	1141	1333	5277	1314	1234	1747	(a)
	Mo	µg L^{-1}	b.l.d.	b.d.l.	b.d.l.	b.d.l.	b.d.l.	b.d.l.	b.d.l.	(a)
	Ni	µg L^{-1}	5	0.4	455	327	181	22	3	(a)
	Pb	µg L^{-1}	3	b.d.l.	22	738	198	6	11	(a)
	Sb	µg L^{-1}	0.5	0.6	1.9	0.5	0.5	2.6	0.1	(a)
	Zn	µg L^{-1}	649	73	29450	27531	14478	607	719	(a)
	La	µg L^{-1}	1.48	0.07	59.8	53.6	17.4	0.13	3.12	(a)
	Ce	µg L^{-1}	3.27	0.39	166.1	105.1	29.1	0.53	1.48	(a)
	Pr	µg L^{-1}	0.31	0.03	15.7	13.4	3.64	0.03	0.17	(a)
	Nd	µg L^{-1}	1.46	0.18	65.2	57.6	13.7	0.28	0.77	(a)
	Sm	µg L^{-1}	0.28	b.d.l.	16.4	15.7	3.42	b.d.l.	0.07	(a)
	Eu	µg L^{-1}	0.02	b.d.l.	4.34	2.84	0.69	0.01	b.d.l.	(a)
	Gd	µg L^{-1}	0.43	0.31	21.4	20.6	4.78	0.21	0.39	(a)
	Tb	µg L^{-1}	0.01	b.d.l.	3.45	3.29	0.78	b.d.l.	b.d.l.	(a)
	Dy	µg L^{-1}	0.20	b.d.l.	14.8	13.2	3.36	0.01	0.09	(a)
	Ho	µg L^{-1}	b.d.l.	b.d.l.	2.72	2.49	0.58	b.d.l.	b.d.l.	(a)
	Er	µg L^{-1}	0.14	b.d.l.	6.39	5.68	1.45	b.d.l.	0.03	(a)
	Tm	µg L^{-1}	b.d.l.	b.d.l.	0.76	0.53	0.10	b.d.l.	b.d.l.	(a)
	Yb	µg L^{-1}	0.02	b.d.l.	4.14	3.35	0.64	0.04	0.05	(a)
	Lu	µg L^{-1}	b.d.l.	b.d.l.	0.49	0.36	0.05	b.d.l.	b.d.l.	(a)
	ΣLREE	µg L^{-1}	6.80	0.67	323.2	245.4	67.3	0.97	5.61	(a)
	ΣHREE	µg L^{-1}	0.82	0.31	58.5	52.3	12.4	0.27	0.56	(a)
	ΣREE	µg L^{-1}	7.62	0.98	381.7	297.7	79.7	1.24	6.17	(a)
	Ratio	-	8.29	2.16	5.53	4.69	5.42	3.59	10.0	(a)
	Ce/Ce*	-	1.10	1.93	1.23	0.89	0.83	1.93	0.46	(a)
	Eu/Eu*	-	0.25	n.d.t.	1.02	0.69	0.75	n.d.t.	n.d.t.	(a)
	$(La/Yb)_N$	-	7.16		1.40	1.55	2.64	0.31	6.05	(a)
	$(La/Gd)_N$	-	0.56	0.04	0.46	0.42	0.59	0.10	1.30	(a)

EC – electric conductivity (values signed with * are in mS cm^{-1}); b.d.l. – below detection limit (< 0.01 µg L^{-1} for all REE element except for Sm (<0.05 µg L^{-1}). (a) – not analysed because the stream was dry; n.d.t. – not determined. Ce/Ce*= the value of the Ce anomaly calculated by the formula $Ce/Ce^* = [(Ce_N)/(SQR(La_N*Pr_N))]$ from Worrall and Pearson, 2001; Eu/Eu*= the value of Eu anomaly calculated by the formula $[Eu/Eu^*]=[(Eu_N)/(SQR(Sm_N*Gd_N))]$ from Worrall and Pearson, 2001. Eu_N, Sm_N, Gd_N = shale-normalized values against NASC

(Gromet et al., 1984). Abbreviations: SW3, SW4, SW6, SW8, SW9, SW12 – samples from Corona stream; SW10 – sample from Lousal stream; SW14 – sample from Sado river.

Table 6
Chemical composition of efflorescent sulphates sampled in the Corona stream and distribution of ΣLREE, ΣHREE, ΣREE, ΣLREE/ΣHREE, Ce/Ce* and Eu/Eu*anomalies, and normalized concentration ratios of $(La/Yb)_N$ and $(Sm/Nd)_N$ in the efflorescent sulfates precipitated in the Corona stream.

Element		**EF1**	**EF2**	**EF3**	**EF4**	**EF5**	**EF6**	**EF7**	**EF8**	**EF9**
Ag	mg kg^{-1}	0.2	0.1	0.1	0.1	0.2	b.d.l.	b.d.l.	b.d.l.	0.7
As	mg kg^{-1}	31	4	35	5	239	752	37	29	411
Bi	mg kg^{-1}	0.5	b.d.l.	0.4	b.d.l.	4.6	13.7	0.2	0.2	5.8
Cd	mg kg^{-1}	18.0	23.9	0.5	18.9	24.1	1.9	9.9	8.8	1.1
Co	mg kg^{-1}	311	342	22	414	458	123	367	349	(a)
Cu	mg kg^{-1}	1966	1185	240	422	1088	641	427	346	243
Mo	mg kg^{-1}	0.3	0.2	0.4	0.2	0.2	0.6	0.2	0.1	0.6
Ni	mg kg^{-1}	143	123	12	152	136	28	180	179	7
Pb	mg kg^{-1}	21	2	70	18	85	14	37	30	357
Sb	mg kg^{-1}	1.2	0.4	8.1	0.1	3.4	1.9	1.0	0.8	10.4
Zn	mg kg^{-1}	7670	9975	313	9311	11250	1090	9669	9602	479
La	mg kg^{-1}	5.50	11.50	14.20	7.70	8.80	1.20	21.70	18.60	17.60
Ce	mg kg^{-1}	12.80	19.30	34.70	11.70	14.10	2.60	47.30	40.90	48.70
Pr	mg kg^{-1}	1.50	2.12	4.31	1.23	1.48	0.30	5.63	4.88	5.93
Nd	mg kg^{-1}	6.90	10.00	19.50	5.30	6.90	1.60	24.50	24.00	27.70
Sm	mg kg^{-1}	2.30	3.20	4.20	1.40	1.90	0.60	6.8	5.90	6.00
Eu	mg kg^{-1}	0.42	0.65	0.54	0.25	0.40	0.13	1.02	0.99	0.73
Gd	mg kg^{-1}	4.40	5.82	3.28	2.22	3.48	0.66	7.73	6.94	5.80
Tb	mg kg^{-1}	0.73	1.00	0.42	0.38	0.57	0.05	1.04	0.84	0.80
Dy	mg kg^{-1}	3.93	5.81	1.90	2.01	3.14	0.39	4.57	3.98	3.35
Ho	mg kg^{-1}	0.80	1.16	0.36	0.40	0.73	0.07	0.80	0.72	0.52
Er	mg kg^{-1}	1.94	2.77	0.80	1.05	1.91	0.17	1.72	1.54	1.16
Tm	mg kg^{-1}	0.25	0.38	0.12	0.11	0.24	b.d.l.	0.21	0.17	0.14
Yb	mg kg^{-1}	1.46	2.15	0.71	0.69	1.27	0.14	1.10	1.10	0.82
Lu	mg kg^{-1}	0.23	0.30	0.12	0.10	0.20	0.02	0.12	0.12	0.10
ΣLREE	mg kg^{-1}	29.0	46.1	76.9	27.3	33.2	6.30	105.9	94.3	105.9
ΣHREE	mg kg^{-1}	14.2	20.0	8.25	7.21	11.9	1.63	18.3	16.4	13.4
ΣREE	mg kg^{-1}	43.2	66.1	85.2	34.5	45.1	7.93	124.2	110.7	119.3
Ratio	-	2.05	2.30	9.32	3.79	2.78	3.87	5.79	5.75	7.89
Ce/Ce*	-	1.01	0.89	1.01	0.86	0.89	0.98	0.97	0.98	1.08
Eu/Eu*	-	0.58	0.66	0.64	0.62	0.68	0.91	0.62	0.68	0.54
$(La/Yb)_N$	-	0.36	0.52	1.94	1.08	0.67	0.83	1.91	1.64	2.08
$(La/Gd)_N$	-	0.20	0.32	0.70	0.56	0.41	0.30	0.46	0.44	0.49

Abbreviations: EF1 – Hexahidrite; EF2 – Rozenite; EF3 – Szomolnokite; EF4 – Rozenite, Alunite, Gypsum, Halotrichite; EF5 – Alunite, Rozenite, Gypsum; EF6 – Copiapite, Coquimbite; EF7 and EF8 – Gypsum, rozenite, alunite, kaolinite; EF9 – Ferrihydrite; b.d.l. (below detection limit); detection limit. Light REE (LREE: La to Sm); Heavy REE (HREE: Eu to Lu); ΣLREE= Sum of total concentration of Rare Earth elements; Ratio = ΣLREE/ΣHREE; Ce/Ce*= the value of the Ce anomaly calculated by the formula $Ce/Ce^* = [(Ce_N)/(SQR(La_N*Nd_N))]$ from Olias et al., 2005; Eu/Eu*= the value of the Eu anomaly calculated by the formula $[Eu/Eu^*]=[(Eu_N)/(SQR(Sm_N*Gd_N))]$ from Olias et al., 2005. Eu_N, Sm_N, Gd_N = shale-normalized values against NASC (Gromet et al., 1984); $(La/Gd)_N$ and $(La/Yb)_N$ are normalized concentration ratios of the selected samples; (a) not analysed

Figure 1

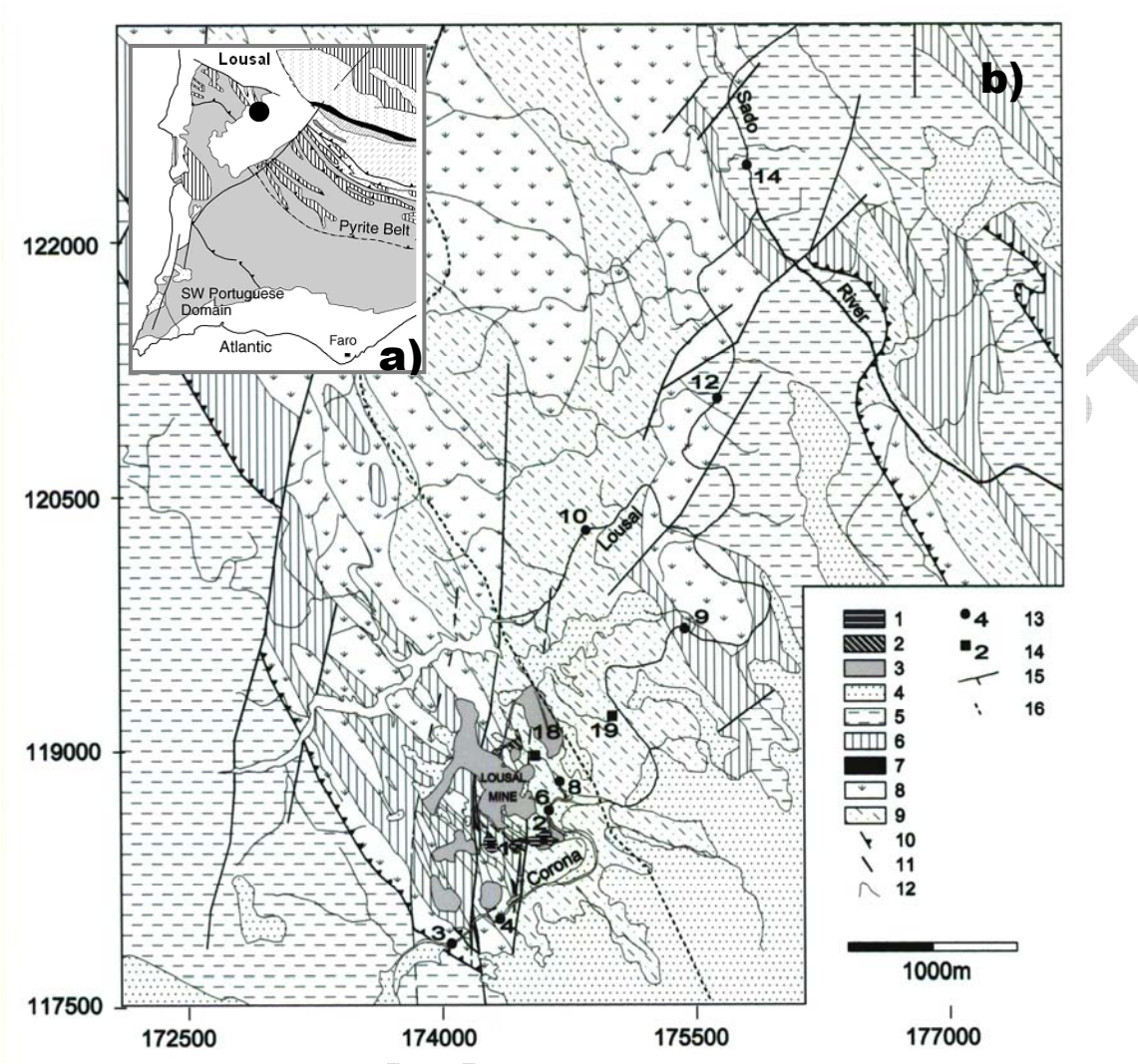

Fig. 1. (a) The NNW Sector of the Iberian Pyrite Belt (adapted from Oliveira *et al.* 2001) (b) Lousal Mine region simplified geological map: 1 – Acid water lagoons; 2 - Acid mine drainage; 3 – Mine waste/contaminated landfill; 4 - Undifferentiated Tertiary Sado Basin and Quaternary alluvionar sediments; Palaeozoic Basement (South Portuguese Zone): 5 - Mértola Fm. (Late Visean); Volcano-Sedimentary Complex (Late Devonian-Late Visean): 6 – VSC sediments; 7 – Massive sulfide ore (Lousal gossans); 8 - VSC volcanics; Phyllite-Quartzite Group (Late Devonian): 9 – Corona Fm. shales and quartzites. 10 – Thrust fault; 11 – Strike-slip fault; 12 – Geological limit. 13 – Sampling site; 14 – AMD source; 15 – Stream; 16 – Railway [ad. Matos 2005, Oliveira et al. 2002]; c) Lousal 3D map showing the abandoned mining area (from http://maps.live.com); T_A and T_B – tailing piles.

Figure 2

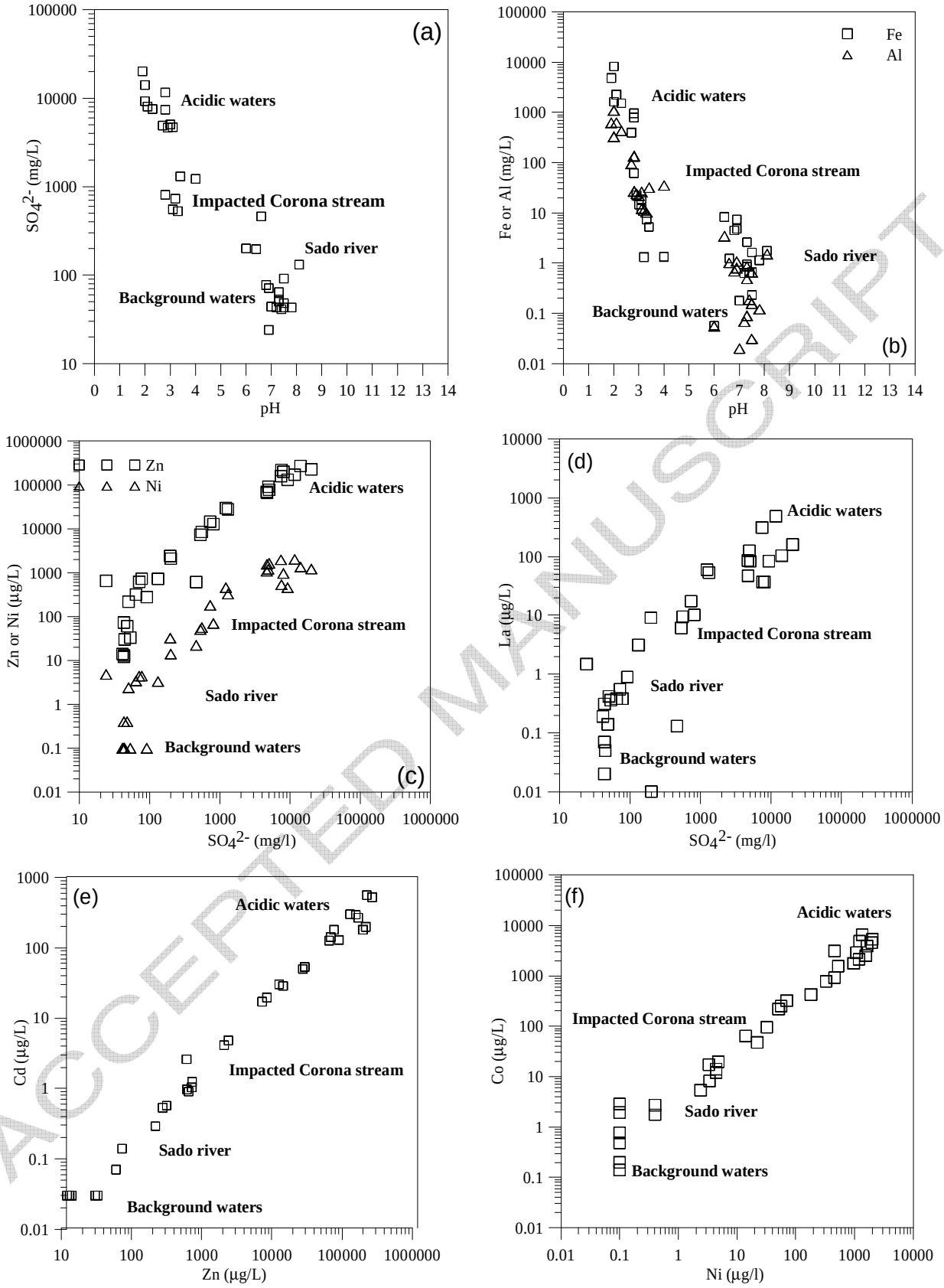

Fig. 2. Binary plots of (a and b) pH versus SO_4^{2-}, Fe and Al, (c and d) SO_4^{2-} versus Zn, Ni and La, (e) Zn versus Cd, (f) Ni versus Co concentrations in the acidic waters (AMW1, AMW2, AMW18, AMW19), impacted Corona stream waters (SW6, SW8, SW9, SW12) and background surface water samples (SW3, SW4, SW10, SW14).

Figure 3

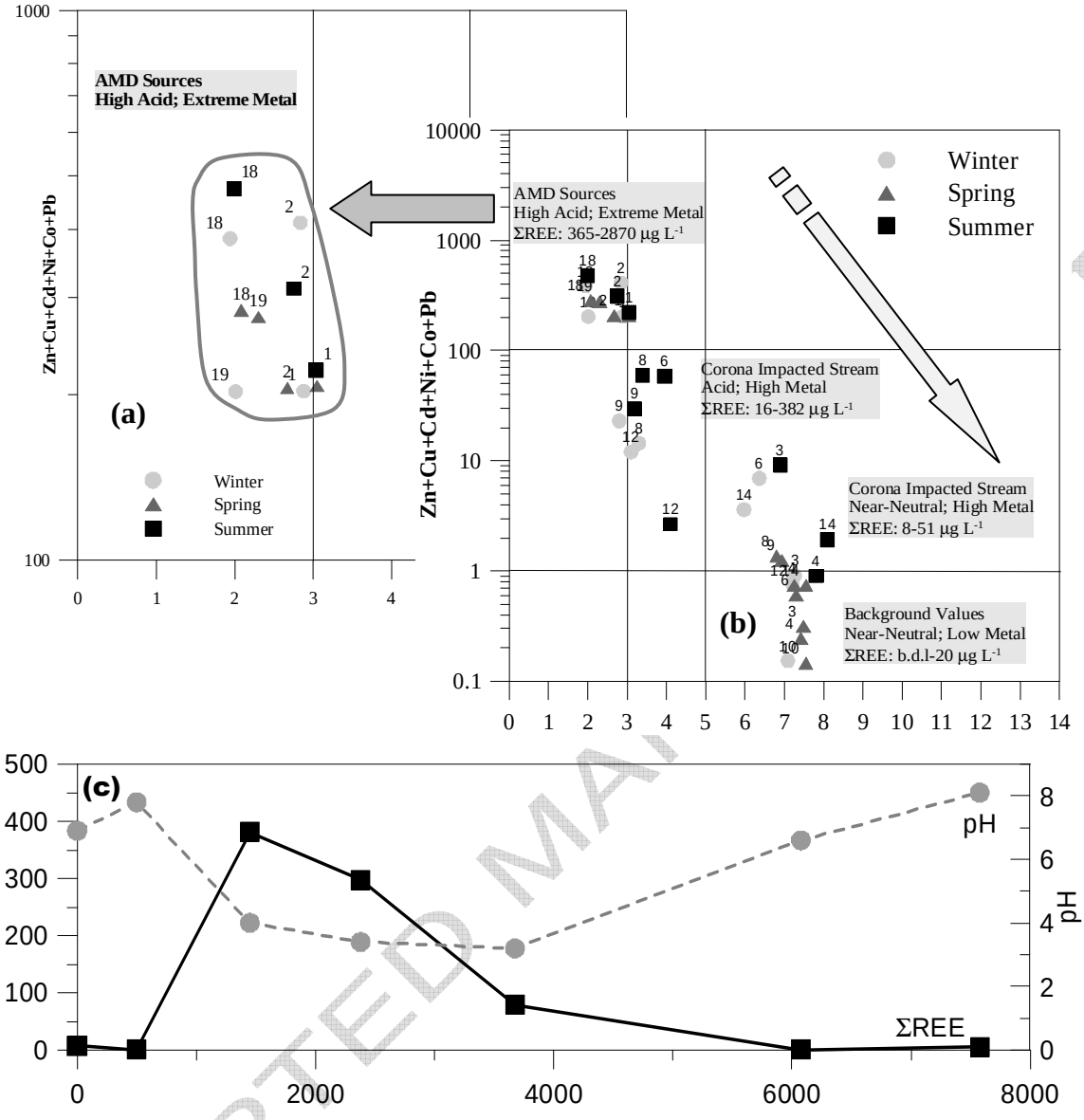

Fig. 3. Ficklin diagram corresponding to water samples collected from Lousal area. (a) Sample label 1 represent the mine lagoon water sample (AMW1), sample label 2 represent the spring water (AMW 2), sample label 18 and 19 represents the flowing channels waters from the tailing piles (AMW18 and AMW19), and (b) sample label 6, 8, 9, 12 the water samples from the impacted Corona stream (SW6, SW8, SW9, SW12), sample label 14 represents the Sado river sample (SW14), and sample label 10 the water sample from Lousal stream (SW10). (c) Plot showing the spatial changes of REE and pH values along the Corona stream.

Figure 4

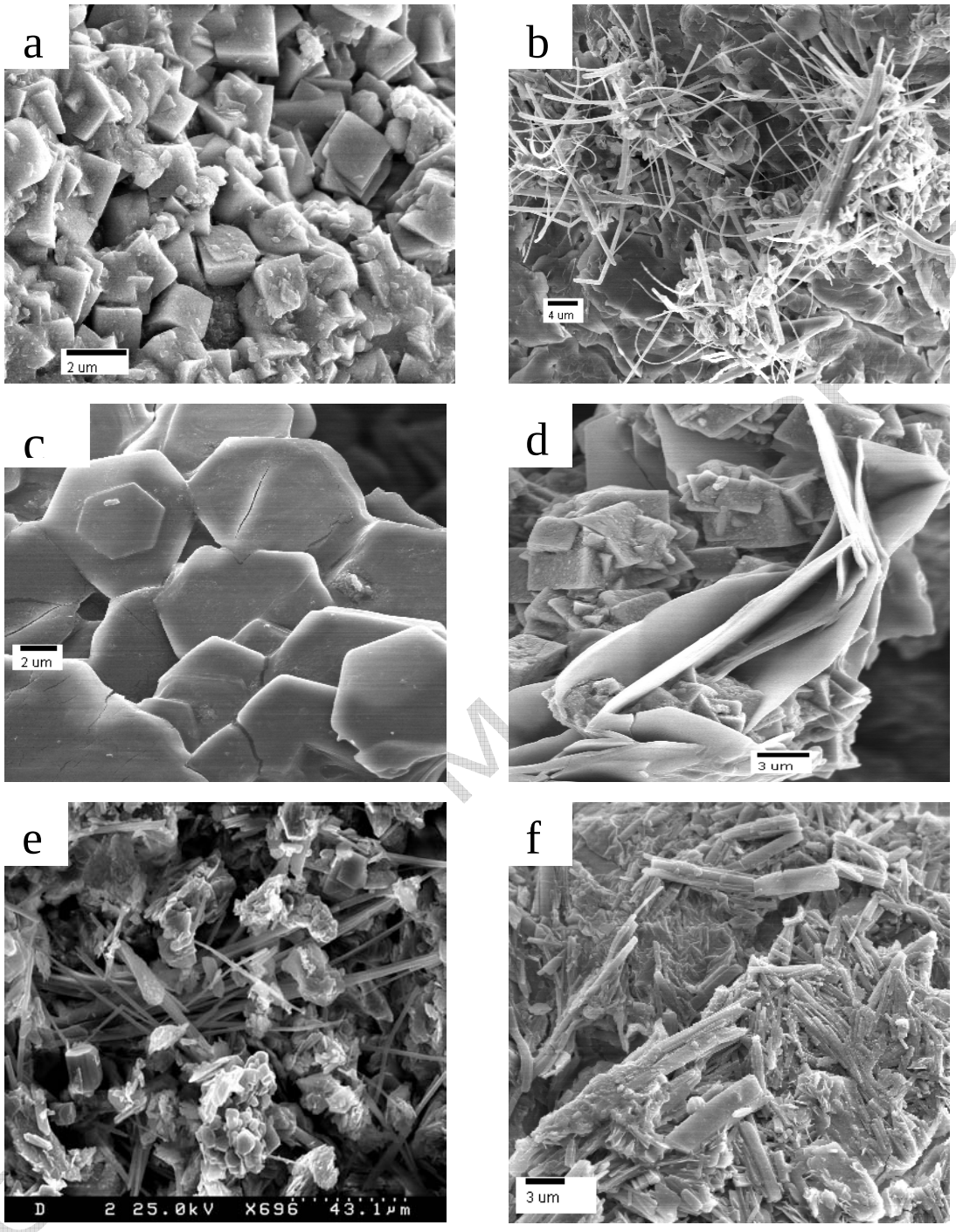

Fig. 4. Scanning electron microscopy images of natrojarosite (a), coquimbite (b and e), Mg-copiapite (c) and Al-copiapite (e), alunite and gypsum (d), halotrickite + pickeringite (f).

Figure 5

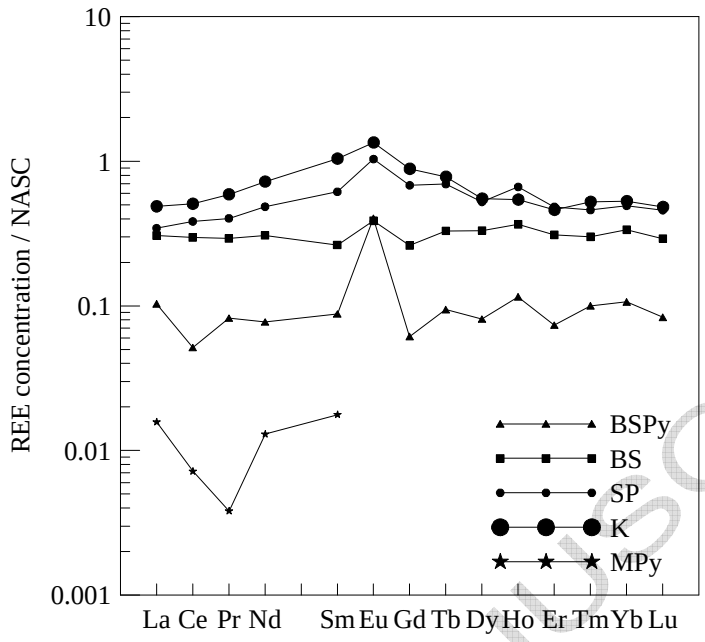

Fig. 5. The NASC normalized distributions of REE of the VMS host rocks and pyrite ore. Abbreviations: BSPy - black shales with pyrite; BS - black shales; SP - spilitic rock; K - kaolin rock; MPy - pyrite.

Figure 6

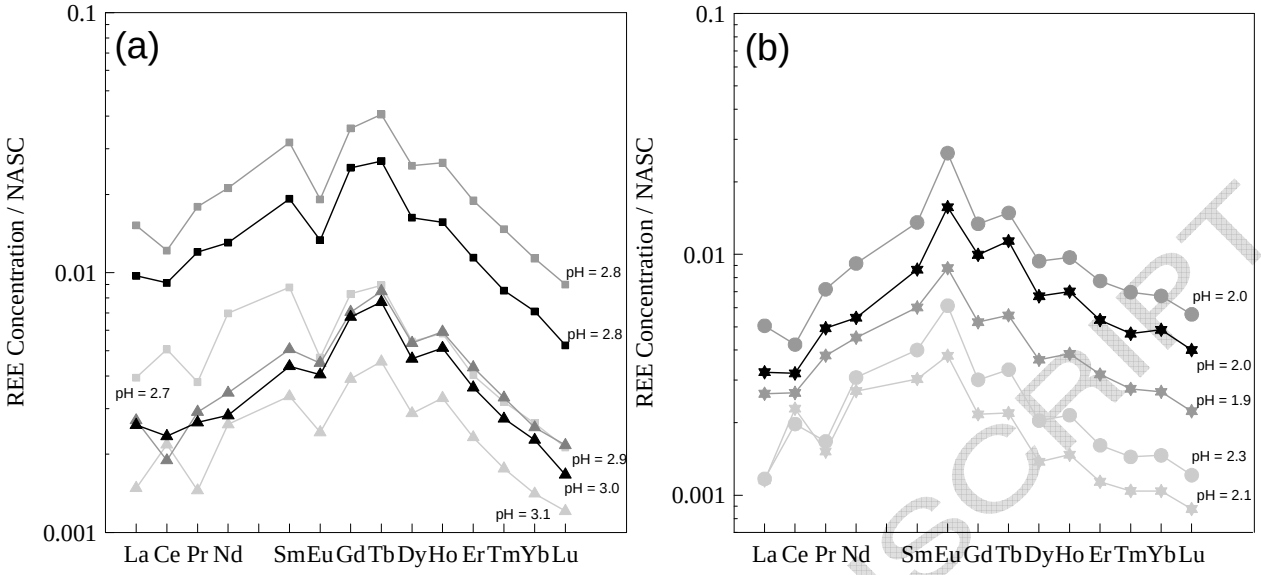

Fig. 6. The NASC normalized REE distribution patterns of acidic mine waters. (a) (▲) AMW1 – Open-pit lake and (■) AMW2 - Acid Spring; (b): (✱) AMW18 - Seeps from tailing T_A and (●) AMW19 - Seeps from tailing T_B. (light gray – winter season; dark gray – spring season; black – summer season).

Figure 7

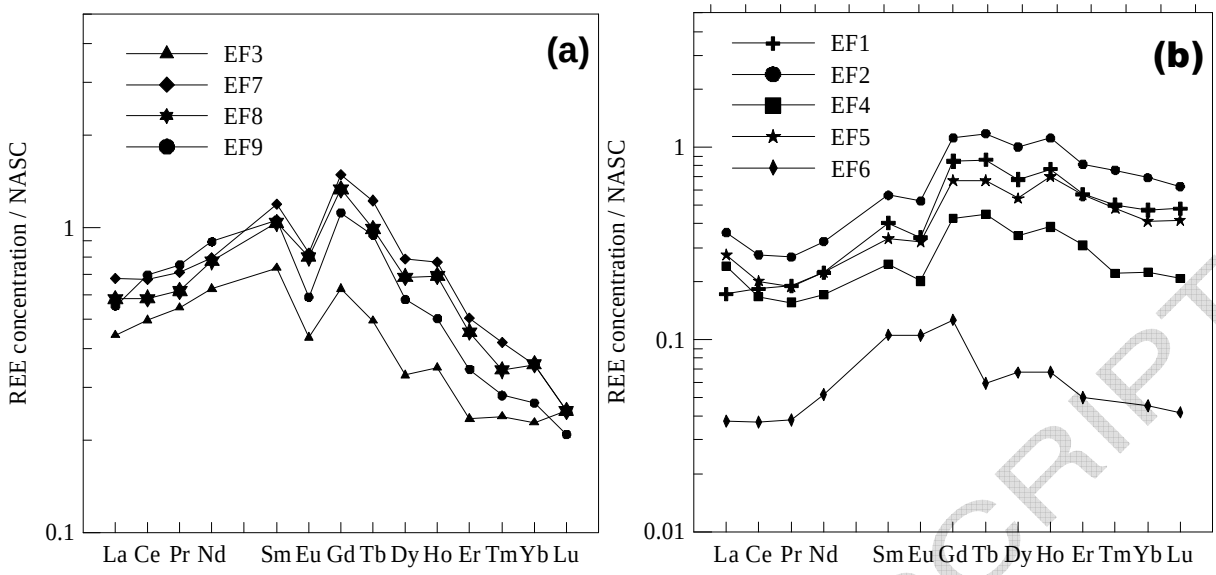

Fig. 7. The NASC normalized REE distribution patterns of efflorescent sulfates formed in the Corona stream. (a) EF3 – Szomolnokite; EF7 and EF8 – Gypsum, rozenite, alunite, kaolinite; EF9 – Schwertmanite; (b) EF1 – Hexahidrite; EF2 – Rozenite, Alunite; EF4 – Rozenite, Alunite, Gypsum, Halotrichite; EF5 – Rozenite, Alunite, Gypsum; EF6 – Copiapite, Coquimbite;

Figure 8

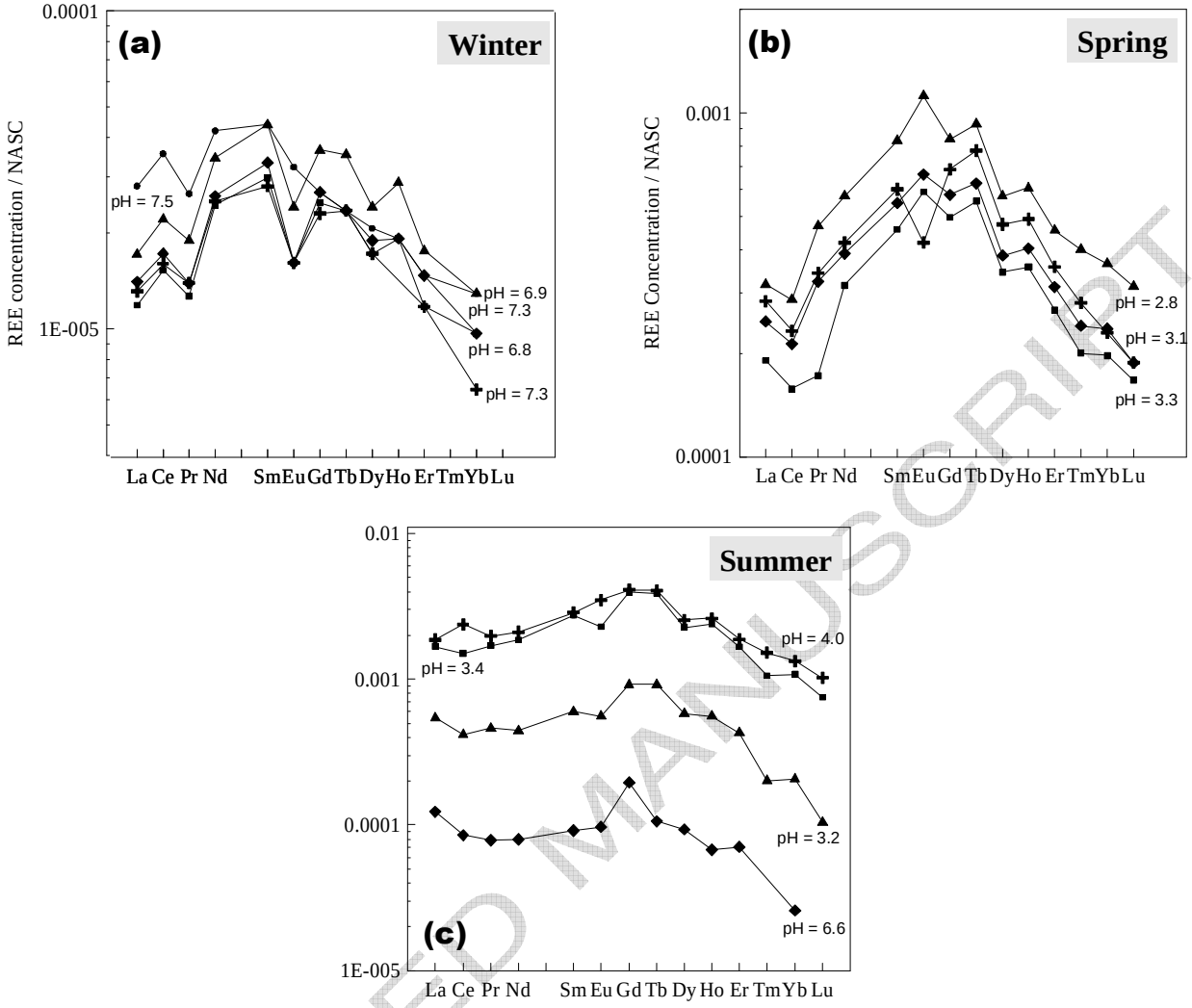

Fig. 8. The NASC normalized REE distribution patterns of stream waters in winter (a), spring (b) and summer (c). Abbreviations: SW6 (+), SW8 (■), SW9 (▲), SW12 (◆) – Corona stream. Samples SW10 (Lousal stream) and SW14 (Sado river) are not plotted because the REE concentrations are below the detection limits.

Figure 9

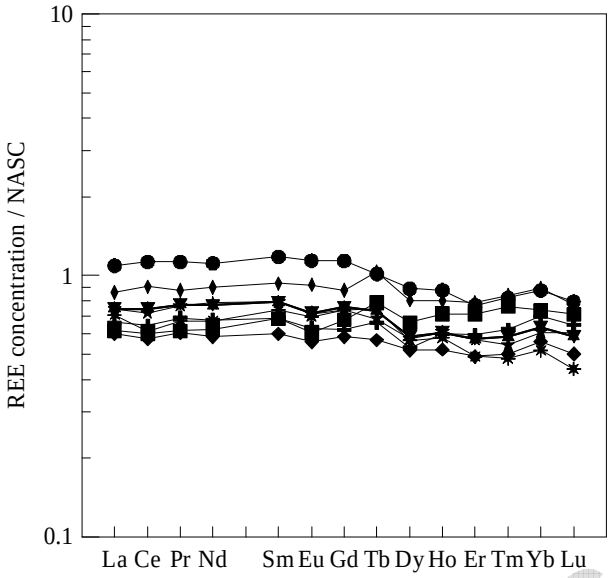

Fig. 9. The NASC normalized REE distribution patterns of the bed-stream sediment samples of the Corona stream - SS3 (▲), SS4 **(▼)**, SS6 (●), SS8 (✱), SS9 (◆), SS12 (⧫) Lousal stream - SS10 (+) and Sado river - SS14(■). The element Pm was not included in the figure because its quantification was not been made.